

A confined dynamo: magnetic activity of the K-dwarf component in the pre-cataclysmic binary system V471 Tauri

Zs. Kővári¹, L. Kriskovics^{1*}, K. Oláh¹, P. Odert^{2,3}, M. Leitzinger^{2,3}, B. Seli¹, K. Vida¹, T. Borkovits^{1,4}, and T. Carroll⁵

¹ Konkoly Observatory, Research Centre for Astronomy and Earth Sciences, Konkoly Thege út 15-17., H-1121 Budapest, Hungary
e-mail: kovari@konkoly.hu

² Institute of Physics/IGAM, University of Graz, Universitätsplatz 5, A-8010 Graz, Austria

³ Space Research Institute, Austrian Academy of Sciences, Schmiedlstraße 6, A-8042 Graz, Austria

⁴ Baja Astronomical Observatory of University of Szeged, Szegedi út, Kt. 766, H-6500 Baja, Hungary

⁵ Leibniz-Institute for Astrophysics (AIP), An der Sternwarte 16, D-14482 Potsdam, Germany

Received ...; accepted ...

ABSTRACT

Context. Late-type stars in close binary systems can exhibit strong magnetic activity owing to rapid rotation supported by tidal locking. On the other hand, tidal coupling may suppress the differential rotation which is a key ingredient of the magnetic dynamo.

Aims. We scrutinize the red dwarf component in the eclipsing binary system V471 Tau in order to unravel relations between different activity layers from the stellar surface through the chromosphere up to the corona. We aim at studying how the magnetic dynamo in the late-type component is affected by the close white dwarf companion.

Methods. We use space photometry, high resolution spectroscopy and X-ray observations from different space instruments to explore the main characteristics of magnetic activity. We apply a light curve synthesis program to extract the eclipsing binary model and further analyze the residual light variations. Photometric periods are obtained using a Fourier-based period search code. We search for flares by applying an automated flare detection code. Spectral synthesis is used to derive or specify some of the astrophysical parameters. Doppler imaging is used to reconstruct surface temperature maps, which are cross-correlated with each other to derive surface differential rotation. We apply different conversion techniques to make it possible to compare the X-ray emissions obtained from different space instruments.

Results. From *K2* photometry we find that 5-10 per cent of the apparent surface of the red dwarf is covered by cool starspots. From seasonal photometric period changes we estimate a weak differential rotation. From the flare activity we derive a cumulative flare frequency diagram which suggests that frequent flaring could have a significant role in heating the corona. Using high resolution spectroscopy we reconstruct four Doppler images for different epochs which reveal an active longitude, that is, a permanent dominant spot facing the white dwarf. From short term changes in the consecutive Doppler images we derive a weak solar-type surface differential rotation with $\alpha_{\text{DR}} = 0.0026$ shear coefficient, similar to that provided by photometry. The long-term evolution of X-ray luminosity reveals a possible activity cycle length of ≈ 12.7 ys, traces of which were discovered also in the $H\alpha$ spectra.

Conclusions. We conclude that the magnetic activity of the red dwarf component in V471 Tau is strongly influenced by the close white dwarf companion. We confirm the presence of a permanent dominant spot (active longitude) on the red dwarf facing the white dwarf. The weak differential rotation of the red dwarf is very likely the result of tidal confinement by the companion. We find that the periodic appearance of the inter-binary $H\alpha$ emission from the vicinity of the inner Lagrangian point is correlated with the activity cycle.

Key words. stars: activity – stars: late-type – stars: imaging – stars: starspots – Stars: individual: V471 Tau

1. Introduction

Magnetic fields have a strong effect on stellar structure and overall, on the long-term evolution of stars, including our Sun. Studying the manifestations of stellar magnetic activity, from photospheric starspots through the bright chromospheric features to the active corona, helps us understand the nature of the underlying magnetic dynamo, and eventually the magnetic evolution of stars. In the last few years it became feasible to study flares on a large number of stars with the *Kepler*, *K2* and ongoing *TESS* missions (e.g. Balona 2015). Such continuous high-precision space photometry combined with high-resolution spectroscopic observations can reveal the connection between the occurrence rate of flares and spot distributions.

It has been learned that late-type stars in close binary systems can exhibit even stronger magnetic activity owing to rapid rotation supported by tidal locking (e.g. Hill et al. 2014). Tidal coupling, however, may suppress the differential rotation (Scharlemann 1982) which is a key ingredient of the magnetic dynamo. In the recent study by Kővári et al. (2017) it was shown that the tidal effect of a close companion star has indeed a suppressive effect on differential rotation.

In our study we scrutinize the red dwarf component in the eclipsing binary system V471 Tau in order to explore relations between different activity layers from the stellar surface through the chromosphere up to the corona. V471 Tau appeared first in the literature as a spectroscopic binary in the General Catalogue of Stellar Radial Velocities (GCVR, Wilson 1953). The system located in the Hyades star cluster consists of DA white dwarf primary with a K2V companion, forming a post-common enve-

* Bolyai János Research Fellow

lope binary (PCEB) star. The age of the Hyades cluster of $t \approx 680$ Myr provides an upper limit for the age of V471 Tau (Gossage et al. 2018). The binary is dubbed to be a pre-cataclysmic variable as well, which means that there is no significant mass transfer in the system, because the K star does not fill its Roche lobe. The orbital period of the eclipsing system of 0.52118 d (for updated orbital parameters see Vaccaro et al. 2015) is modulated on the long term, which was explained by a light-time effect due to the gravitational influence of a third body, possibly a brown dwarf (Guinan & Ribas 2001). As an alternative explanation, the Applegate mechanism was offered by Hardy et al. (2015), where eclipse timing variations were interpreted as changes in the quadrupole moment within the K2V star. Recently, Lanza (2020) has proposed a mechanism based on a permanent non-axisymmetric gravitational quadrupole moment. It is no exaggeration to say that V471 Tau is an actual astrophysical laboratory for studying many aspects of stellar evolution. The white dwarf primary with a surface temperature of ≈ 35000 K has strong emission in the ultraviolet (UV), extreme ultraviolet (EUV) and X-ray regimes. In such PCEB systems X-ray emission can originate from either the white dwarf or the corona of the K star. Moreover, the hot primary can also heat the exposed hemisphere of the secondary. V471 Tau is a well-known variable at the high energy electromagnetic regime as well, being observed during the *Einstein* (Young et al. 1983), *IUE* (Guinan & Sion 1984), *EXOSAT* Jensen et al. (1986), *ROSAT* (Barstow et al. 1992; Wheatley 1998) and more recently in the course of *Chandra* (García-Alvarez et al. 2005) and *XMM Newton* missions, to mention the most important ones. Accordingly, among other major findings, Jensen et al. (1986) discovered the pulsation of the white dwarf, while (Barstow et al. 1992) confirmed a weak accretion from the K star to the white dwarf via stellar wind. Using *UV* data from Goddard High Resolution Spectrograph (GHRS) on board the *Hubble Space Telescope* Bond et al. (2001) reported Coronal Mass Ejections (CMEs) from the active K dwarf and estimated a 100-500 CMEs per day emission rate, i.e. about a hundred times higher frequency compared to the Sun.

As for the surface magnetic activity of the secondary, the K2V star, forced to rotate synchronously with the orbital period, is known to exhibit rotational variability due to starspots (e.g. Evren et al. 1986) and flare activity (Young et al. 1983). The first Doppler images of the star were presented by Ramsayer et al. (1995), who obtained four separate temperature maps spanning over a year. In another Doppler-imaging study Hussain et al. (2006) found that despite the tidally inhibited differential rotation the K-dwarf component of the V471 Tau binary system showed indeed a high level of magnetic activity. In our paper we perform a complex study of the magnetic activity of V471 Tau, including new Doppler images and flare statistics for the spotted red dwarf.

The paper is organized as follows. In Sect. 2 we summarize the available photometric and spectroscopic data to be analyzed. Using *Kepler K2* observations, in Sect. 4 by extracting orbital solution we analyze light variations due to spots and flares. In Sect. 3 by the means of spectral synthesis we derive precise astrophysical parameters of the active K-dwarf component, which is used to perform a Doppler imaging study in Sect. 5 where we estimate the surface differential rotation of the spotted star. The chromospheric and coronal activity of the K star is analyzed in Sect. 6.2. Our results are discussed in Sect. 7 and summarized in Sect. 8.

2. Data

2.1. *K2* photometry

The *Kepler K2* mission provided long-term high-precision space photometry (Howell et al. 2014) of V471 Tau (EPIC 210619926). The star was observed as part of the 4th Campaign of the mission between 08 February–20 April 2015 (BJD 2457061.7910–2457132.6877), covering 136 subsequent orbital cycles. Both short (1-min) and long cadence (30-min) light curves of V471 Tau are available for the interval. Although the *K2* data do not coincide with the spectroscopic observations used in this paper, the short cadence space data are suitable for studying spot evolution and flare activity on a somewhat longer timescale. As an example, in Fig. 1 we plot a two cycles long part of the short cadence light curve, where in-eclipse and out-of-eclipse flares are also seen.

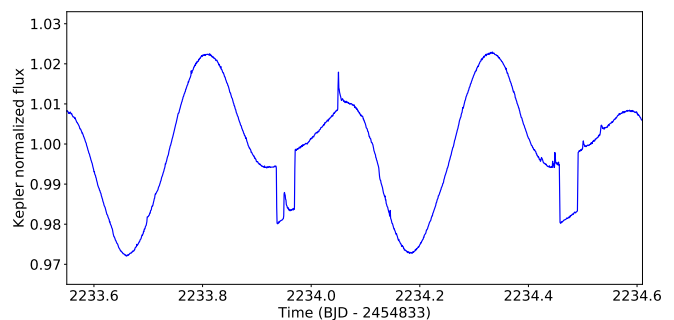


Fig. 1. Part of the *Kepler K2* short cadence data of V471 Tau with a particular flare event occurred when the white dwarf component was in eclipse.

2.2. High-resolution spectroscopy

We use high-resolution ($R=81000$) spectroscopic observations of V471 Tau publicly available in the data archive of the Echelle SpectroPolarimetric Device for the Observation of Stars (ESPaDOnS) at Canada–France–Hawaii Telescope (CFHT). The spectra cover the 3700–10500 Å optical range. The available data were retrieved in two seasons, the first in December 2005 and the second at the turn 2014/2015. We selected 297 and 222 spectra from the two seasons, respectively, to achieve uttermost subsets (in the long run two in both seasons) with regard to optimal phase coverage for Doppler imaging (see Sect. 5). Low quality spectra with signal-to-noise $S/N < 40$ were omitted from the selection. Before using the four data subsets for Doppler image reconstructions we shifted the spectra to the rest wavelength and continuum fitting was carried out. The CFHT spectra contain the $H\alpha$ region which is used to study the chromospheric activity and discover possible mass motions in the binary (see Sec. 6.1). The observing log of the CFHT-ESPaDOnS spectra used in our study is given in Table A.1 in Appendix A.

2.3. X-ray observations

The V471 Tau system has been detected with many X-ray instruments during the last decades. Here we attempt to infer the long-term variability of the K dwarf’s coronal emission. As none of the X-ray observations coincide with the epochs of the high resolution spectroscopic data for Doppler imaging, we do not address its variability on shorter timescales like rotational modulation

due to the distribution of active regions. We note that the binary components are not spatially resolved in the X-ray observations, but it is well established that only the softer ($> 50\text{\AA}$) wavelength range is affected by the emission from the white dwarf (Drake & Sarna 2003; García-Alvarez et al. 2005), therefore its eclipse (at $\phi=0$ orbital phase) is only observed in soft X-ray/EUV light curves (Cully et al. 1996; Wheatley 1998). What makes the investigation of the long-term coronal variability difficult is that V471 Tau was rarely observed by the same instrument more than once, the only exception being the *ROSAT* pointed survey (twice during the same year) and *XMM Newton* (separated by 15 years). Moreover, the K dwarf is very active due to its high rotation rate, so its emission is variable also on short time scales, including frequent flares, which makes the definition of a quasi-quietest emission level during a given epoch difficult.

For the analysis we select data from five X-ray instruments covering the years 1991–2019 (Table 1). We do not include data from earlier instruments (*Exosat*, *Einstein*) and the *ROSAT* All Sky Survey (RASS), because of their softer wavelength coverage (including mainly the white dwarf’s emission) and/or their short duration (RASS). When selecting the space data we considered the epochs of our new Doppler reconstructions as well (see Sect. 5). In Sect. 6.2 we describe the detailed analysis steps for each instrument and observation, as well as which data were taken from previous analyses in the literature.

3. Stellar properties

3.1. Adopted parameters

The *Gaia* DR2 parallax of $\pi = 20.957 \pm 0.044$ mas (Gaia Collaboration et al. 2018) yields a distance of $d = 47.72 \pm 0.10$ pc for V471 Tau. This distance assuming $V_{br} \approx 9^m35$ for the brightest V magnitude observed so far in 2004 (cf. İbanoğlu et al. 2005) and removing $\Delta V_{wd} = -0^m02$ as the contribution of the white dwarf (Rucinski 1981) and taking into account a maximum of $A_V = 0^m003$ interstellar extinction (cf. Taylor 2006) yields an absolute visual magnitude $M_V = 5^m97 \pm 0^m03$. Taking $BC = -0.257$ bolometric correction from (Flower 1996) gives a bolometric magnitude $M_{bol} = 5^m72 \pm 0^m03$. This gives $L/L_{\odot} = 0.41 \pm 0.01$ when using $M_{bol,\odot} = 4^m74$ value for the Sun. On the other hand, when adopting $R/R_{\odot} = 0.91 \pm 0.02$ (Vaccaro et al. 2015, see their Table 11) and with $T_{eff} = 4980$ K (see Sect. 3.2) the Stefan–Boltzmann law would give a bit higher L/L_{\odot} ratio of 0.46 ± 0.04 ; still in a fair agreement with the value obtained from the bolometric magnitude.

We perform a spectral energy distribution (SED) synthesis using the virtual observatory (VO) tool VOSA (Bayo et al. 2008) to build the SED of V471 Tau from the available VO catalogs. We use VOSA to collect archival photometry from *Tycho*, *SLOAN/SDSS*, *Gaia* DR2, *2MASS*, *AKARI/IRC*, and *WISE* surveys. As input we confined the effective temperature to $4950\text{ K} < T_{eff} < 5050\text{ K}$, the surface gravity to $4.25 < \log g < 4.75$, and the metallicity to $-0.2 < [\text{Fe}/\text{H}] < 0.2$ (cf. Sect. 3.2). The resulting synthetic spectrum plotted in Fig. 2 corresponds to L/L_{\odot} of 0.40 ± 0.21 , in agreement with both values given hereinabove.

The $v \sin i = 91\text{ km s}^{-1}$ projected rotational velocity of the K2 star was adopted from Hussain et al. (2006, see also their references). The inclination $i = 77^{\circ}4^{+7.5}_{-4.5}$ of the binary orbit with respect to the line of sight was derived in O’Brien et al. (2001), which we adopt here for the K-dwarf with the assumption that its rotational axis is perpendicular to the orbital plane.

Adopting $P_{orb} = P_{rot}$ period and $\text{HJD}_0 = 2440610.06406$ reference time (mid-primary minimum, when the white dwarf is

in eclipse) from Guinan & Ribas (2001) we use the following equation for calculating the phase values of the spectroscopic observations in Table A.1:

$$\text{HJD}_{\phi=0} = 2440610.06406 + 0^d521183398 \times E. \quad (1)$$

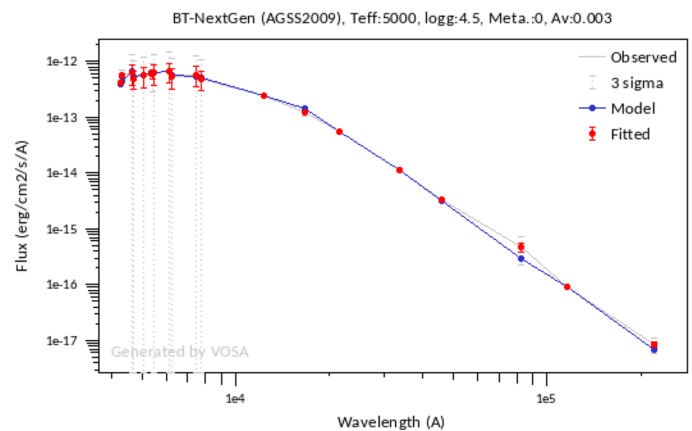


Fig. 2. Spectral energy distribution for V471 Tau generated by the VOSA SED analyzer tool (Bayo et al. 2008). The synthetic spectrum (blue line) is fitted to the available archival photometry (red dots) from *Tycho*, *SLOAN/SDSS*, *Gaia* DR2, *2MASS*, *AKARI/IRC*, and *WISE* surveys.

3.2. Spectral synthesis

We carried out a detailed spectroscopic study based on spectral synthesis using the code SME (Piskunov & Valenti 2017). During the synthesis, MARCS models were used (Gustafsson et al. 2008) and atomic parameters were taken from VALD (Kupka et al. 1999). Macroturbulence was computed using the following equation from Valenti & Fischer (2005):

$$v_{mac} [\text{km s}^{-1}] = 3.98 - \frac{T_{eff} [\text{K}] - 5770}{650}. \quad (2)$$

First, we selected 15 good quality spectra observed in eclipses, when only the K2 star was seen, and performed the synthesis independently for the 15 spectra to get T_{eff} , $\log g$, and $[\text{Fe}/\text{H}]$. We used the initial values as input for subsequent iterations. We gradually confined the microturbulence and the projected rotational velocity at $v_{mic} = 0.7(\pm 0.2)\text{ km s}^{-1}$ and $v \sin i = 91(\pm 1)\text{ km s}^{-1}$, respectively, in agreement also with literary values (cf., e.g., Hussain et al. 2006; Adibekyan et al. 2012, and their references). Finally, the surface gravity was kept fixed at $\log g = 4.5$, in agreement with former, well established values (see Vaccaro et al. 2015, and their references). At the end, the procedure resulted in $T_{eff} = 4980\text{ K}$ and $[\text{Fe}/\text{H}] = 0.12$. For details of the iterative fitting method see Kriskovics et al. (2019). The final astrophysical parameters with their errors are listed in Table 2.

In the second test we run the synthesis for all the available CFHT spectra to see if the surface temperature varies along the orbital phase. Therefore, all of the previously derived parameters were kept fixed except for the surface temperature. The results are plotted in Fig. 3, demonstrating that the surface of the red dwarf is indeed the least affected around $\phi = 0.0$ when the hot component is obscured. The temperature rise of $\approx 100\text{ K}$ at $\phi = 0.5$ compared to the eclipse either in 2005 (blue dots in the figure) or 2014/15 (red dots) may be due to the irradiation of

Table 1. Adopted X-ray observations of V471 Tau with their durations and the quiescent periods within them

Date [dd.mm.yyyy]	Mission	Instrument	Observing ID	Duration [s]	Quiet [s]
23.08.1991	<i>ROSAT</i>	PSPC	RP200107M01	27692	all
26.08.1996	<i>ASCA</i>	SIS+GIS	24032000	102416	all
14.08.1997	<i>ROSAT</i>	HRI	RH202309N00	15793	1104
24.01.2002	<i>Chandra</i>	HRC-S/LETG	2523	87990	all
01.08.2004	<i>XMM Newton</i>	EPIC/PN	0203260101	60924	18783
30.07.2015	<i>Swift</i>	XRT	33909	2447	all
04.09.2019	<i>XMM Newton</i>	EPIC/PN	0844350101	63500	9381

the hot component, but surface activity can also play a role (see Sect. 7.2 for a discussion). Indeed, it is very likely that the stellar dynamo in the synchronously rotating red dwarf is affected by the close companion and therefore manifestations of magnetic activity may be coupled to the orbital phase (cf. Schrijver & Zwaan 1991).

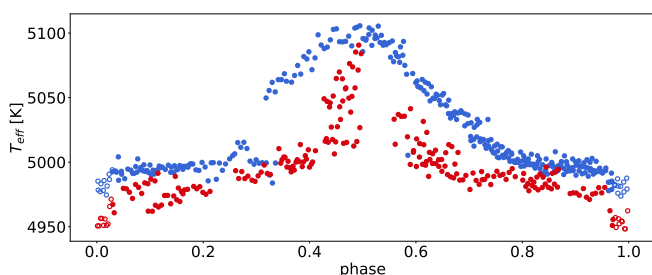


Fig. 3. Variation of the surface temperature of the K2 star along the orbital phase. Dots show the temperature values derived individually for each spectra (blue for the 2005 season, red for the 2014/15 spectra) by spectral synthesis. Open circles around zero phase correspond to those unaffected spectra that were observed when the white dwarf was eclipsed. The temperature rise of ≈ 100 K at $\phi \approx 0.5$ in both seasons may indicate the irradiation effect of the hot component. See Sect. 3.2 for details.

Table 2. Fundamental astrophysical data of the K2 dwarf component of V471 Tau

Parameter	Value
Spectral type	K2 V
Gaia distance [pc]	47.72 ± 0.10
V_{br} [mag]	$9^m37 \pm 0^m03$
M_{bol} [mag]	5.72 ± 0.03
Luminosity [L_{\odot}]	0.41 ± 0.01
T_{eff} [K]	4980 ± 10
$\log g$ (in cgs)	4.50 ± 0.05
[Fe/H]	0.12 ± 0.04
v_{mic} [km s^{-1}]	0.7 ± 0.2
v_{mac}^a [km s^{-1}]	5.2
$v \sin i$ [km s^{-1}]	91 ± 1
Rotation period [d]	0.521183398
Inclination ^b [$^{\circ}$]	$77.5^{+7.5}_{-4.5}$
Radius ^c [R_{\odot}]	0.91 ± 0.02
Mass ^c [M_{\odot}]	0.95 ± 0.05

Notes. ^(a) Computed using Eq. 2; ^(b) O’Brien et al. (2001); ^(c) Vaccaro et al. (2015).

4. Photometric analysis

4.1. Extracting the eclipsing binary light curve

Before analyzing the photometric signs of the magnetic activity of V471 Tau we removed the light curve variations caused by the close binary nature as follows. First, we formed a phase-folded light curve with the use of the *K2* short cadence light curve. The data were grouped into 2000 orbital phase bins of equal duration. Then, the average of each phase cells were calculated and rendered to the mid-phase point of the given cell. This way the fastest part of the non-orbital phase-locked light variations were removed, but a significant amount of the intrinsic variability over longer timescales has remained in the light curve. In order to remove these slower variations we synthesized a pure binary light curve with the use of the software package *Lightcurvefactory* (Borkovits et al. 2020). The input parameters were taken from Vaccaro et al. (2015). Besides the eclipses, the binary model has included ellipsoidal variations and the effect of Doppler-boosting, too. We did not consider, however, the reflection/irradiation effect of which the photometric contribution was found to be negligible. Using the parameters from Vaccaro et al. (2015, see their Table 8, 4th column) after a natural readjustment of the mid-time of a given eclipse (T_0) parameter to the value appropriate for *K2* data and comparing the synthesized light curve against the folded, binned, averaged *K2* light curve, the residual curve has shown significant shoulders around the partial phases of the eclipses, revealing, that the durations of both the total eclipses and the totality should slightly be readjusted. We made it manually with slight modifications of the radius of the K dwarf component. This way we were able to remove the shoulders from the residual file. Finally, with a repeated use of *Lightcurvefactory*, this slightly refined synthetic light curve was removed from the original, ≈ 71 d long *K2* measurements. The resulting residual light curve is plotted in Fig. 4.

4.2. Analyzing spot variability

According to Fig. 4 the light curve is solidly modulated by a continuously changing spot distribution. The relative intensity of the spot amplitude varies between 0.03-0.06. From this we estimate that 5-10 per cent of the apparent stellar surface is covered by spots (see Eq. 3 in Notsu et al. 2019). Assuming surface differential rotation, the change in the rotational frequency signals can be interpreted as a change in the latitude of the dominant surface spots. To recover the presence of differential rotation from the 136-cycle (≈ 71 -day) long photometric time series we apply the following technique. First, the entire residual light curve (bottom panel of Fig. 4) was divided into eight consecutive sections of ≈ 9 -day long (17 rotational cycles), i.e., a compromise to avoid averaging frequency signals over a longer time scale but still get stable/reliable frequencies for the given part. To derive

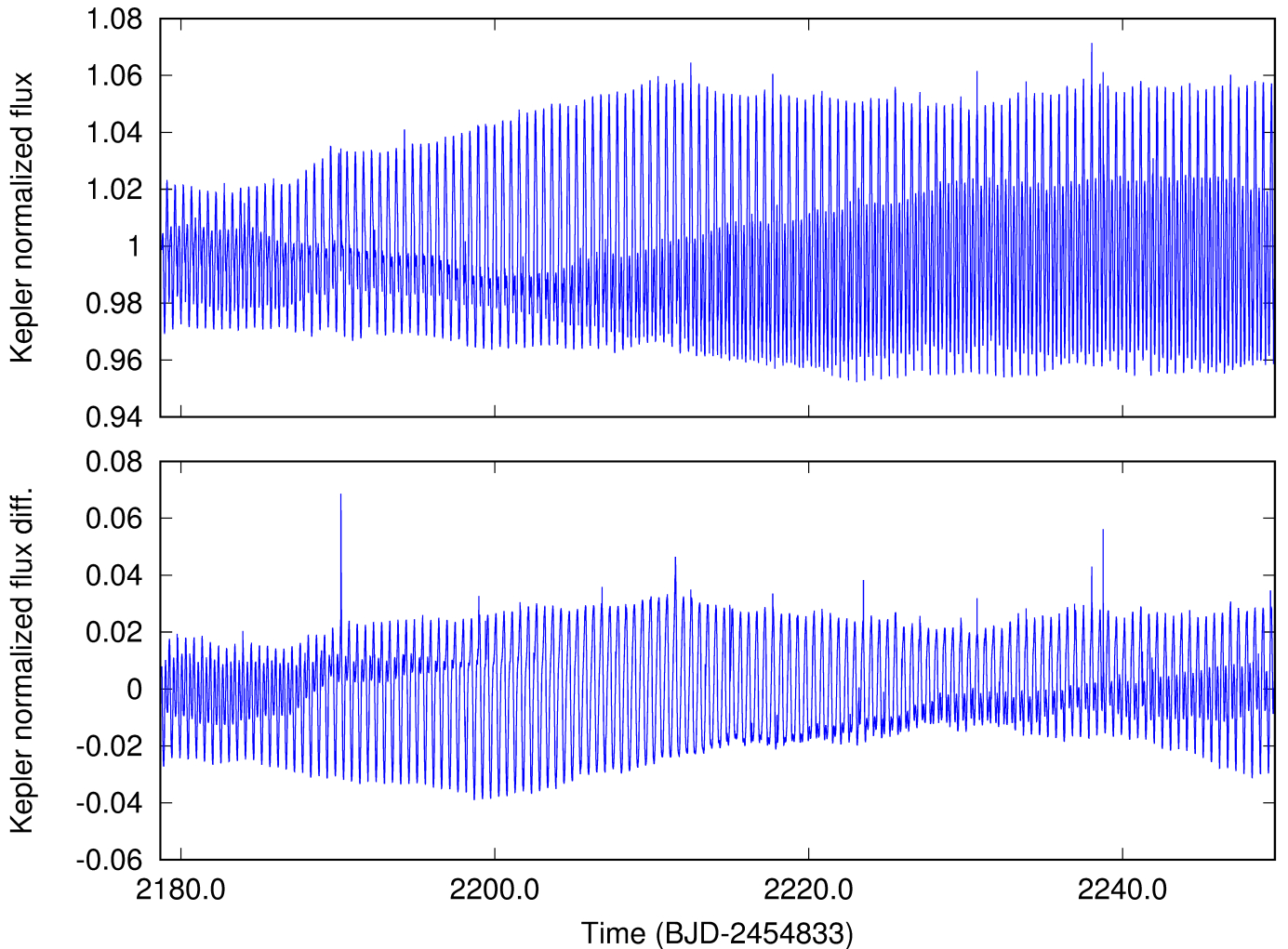


Fig. 4. *K2* light curve of V471 Tau (top) and residual light variations (bottom) due to spots and flares after extracting the eclipsing binary model. See Sect. 4.1 for details.

the most characteristic rotational period for each part we apply the Fourier-based period search code MuFrAn (Csubry & Kol-láth 2004). The resulting short term rotational periods listed in Table 3 indicate that the change in the period remains within a narrow interval of $\Delta P \approx 0.001$ day. Dividing this by the average rotation period from Table 2, we can estimate the dimensionless surface shear coefficient as $|\alpha_{\text{DR}}| \gtrsim \Delta P_{\text{phot}}/\bar{P}$, where ΔP_{phot} is the full range of the seasonal photometric period associated with surface spots, while \bar{P} is the average period over long term. From the values listed in Table 3, we obtain $|\alpha_{\text{DR}}| \gtrsim 0.002$, i.e., a weak shear, almost solid-body rotation. We note, that this method alone does not allow to determine the sign of the surface shear parameter, i.e., whether the differential rotation is solar type or antisolar.

4.3. Finding flares

After extracting the eclipsing binary model from the *K2* light curve we search for flares in residual time series (bottom panel of Fig. 4.1) by applying the automated flare detection code FLATW'RM (FLAre deTectioN With Ransac Method, Vida & Roettenbacher 2018). The code enables the user to adjust the detection level and the number of successive points associated with a given flare. This is especially important when detecting the

Table 3. Seasonal photometric periods from *K2* data

Season No.	BJD start ^a	BJD end ^a	P_{phot} [d]
1	2228.790988	2236.999957	0.520938
2	2237.000638	2245.999560	0.520565
3	2246.000241	2254.999765	0.520193
4	2255.000446	2263.999913	0.520645
5	2264.000594	2272.999345	0.520336
6	2273.000026	2281.999446	0.519983
7	2282.000127	2290.999555	0.520641
8	2291.000236	2299.687090	0.519987

Notes. ^(a) +2454833.0

smallest events just above the noise level, which are always difficult to find. However, close to the noise limit the number of false positives is starting to increase, which, on the other hand, can be compensated by increasing the number of associated points. After a visual inspection, however, we declared 15 false positives among the detected events. On the other hand, a similar number of possible flares just above the noise level could have been missed. Due to these reasons, we ran a second analysis using a flare-searching neural network (Vida et al., in prep.), and cor-

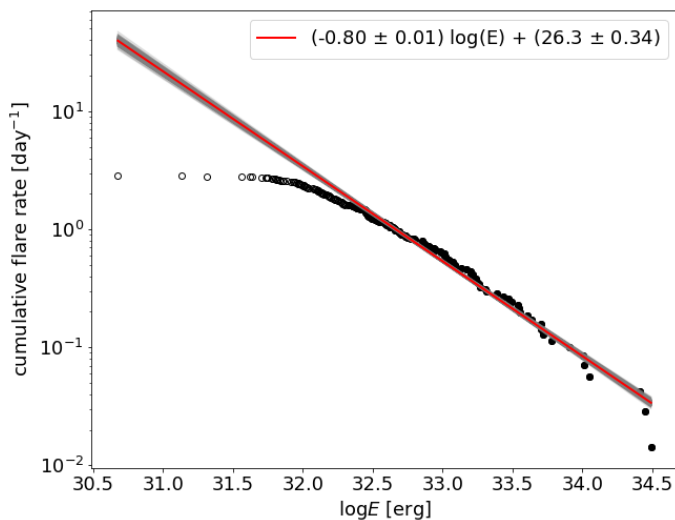


Fig. 5. Cumulative flare-frequency diagram for V471 Tau. The slope of the linear fit (orange line) corresponds to $\alpha = 1.8$ power law index.

rected its output manually for possible false positive/negative detections. This analysis yielded a final number of 198 confirmed flare events in the 71-day long *K2* time series.

Taking T_{eff} and R from Table 2 the blackbody approximation yields $L_q = 4.64 \times 10^{32} \text{ erg s}^{-1}$ quiescent luminosity for the K dwarf through the *Kepler* filter. To determine the individual flare energies, first, the background variation (due to spots) is removed by fitting a low-order polynomial to the 1 hour interval of the given flare (omitting the flaring points). The order of the polynomial is determined by the Bayesian Information Criterion. After subtracting this polynomial, the net flare light curve is integrated over the duration of the flare, yielding the ε_f relative flare energy (or equivalent duration) of the event. Multiplying ε_f with L_q gives the total energy E_f released by the flare. Finally, E_f values are used to make up the cumulative flare frequency diagram in Fig. 5.

In principle, the cumulative number of flares vs. flare energy can be described by a power law (Gershberg 1972). Accordingly, the logarithm of the $\nu(E)$ cumulative number of flares with energy values larger than or equal to E can be written as:

$$\log \nu(E) = c_1 + c_2 \log E, \quad (3)$$

where c_1 is the intercept while c_2 is the slope of a linear function. Rewriting the slope $c_2 = 1 - \alpha$ one can introduce α , that is the power law index of the flare energy distribution (Hawley et al. 2014). The low energy turnover of the diagram below $\log E \approx 32.6$ [erg] is most probably the result of the detection threshold. Fitting the distribution above this turnover (see the red line in Fig. 5) yields a power law index of $\alpha = 1.80 \pm 0.01$. For further discussion about the flare statistics see Sect. 7.3.

5. Doppler imaging

5.1. The state-of-the art imaging code *iMap*

To reconstruct the surface temperature distribution map of V471 Tau we use the Doppler imaging code *iMap* (Carroll et al. 2012). This state-of-the-art code carries out multi-line inversion on a list of photospheric lines between 5000–6750 Å. We selected 24 non-blended absorption lines with suitable line-depth, temperature sensitivity and well defined continuum. The stellar surface is modelled on a $5^\circ \times 5^\circ$ resolution grid. Each local line

profile is computed with a full radiative solver (Carroll et al. 2008). The local line profiles are disk integrated, and the individually modelled, disk-integrated lines are averaged. Atomic line data are taken from the Vienna Atomic Line Database (VALD Kupka et al. 1999). Model atmospheres are taken from Castelli & Kurucz (2004) and are interpolated for the necessary temperature, gravity or metallicity values. When solving the radiative transfer local thermodynamical equilibrium (LTE) is assumed because spherical model atmospheres would have required too much computational capacity. Nevertheless, imperfections due to the LTE approximation in the fitted line shapes are well compensated by the multi-line approach. Additional input parameters are micro- and macroturbulence, and the projected equatorial velocity (cf. Sect. 3).

For the surface reconstructions *iMap* uses an iterative regularization based on a Landweber algorithm (Carroll et al. 2012). The iterative regularization has been proven to converge always on the same image solution (for the tests see Appendix A in Carroll et al. 2012). Therefore, no additional constraints are imposed for the image reconstruction.

5.2. Surface temperature maps

In order to achieve good enough phase coverage for the ≈ 0.52 day rotational period, we decided to form two subsets for both observing seasons. The first two sets for the 2005 season, henceforth S1 and S2, consist of 149 and 172 spectra, respectively, both covering roughly four rotations (≈ 2 days). The S3 and S4 subsets for the 2014/15 season consist of 131 and 97 spectra, respectively, however, due to unfavourable data distribution in this season the S3 subset covers ≈ 20 consecutive rotations (≈ 10 days) while S4 covers ten rotations (5 days); see Table A.1 in the Appendix. All four subsets are used to reconstruct one Doppler image. The mean HJDs for the four subsets are 2453719.705, 2453722.211, 2457016.565, and 2457031.375, respectively. The four Doppler images (referred hereafter as S1, S2, S3 and S4) presented below, can be regarded as "snapshots" of the stellar surface at these times.

5.2.1. Doppler images from the 2005 CFHT spectra

In Fig. 6, the two subsequent Doppler maps for the 2005 season (S1, S2) are plotted in orthographic projection in the quadrant phases of the rotation. The corresponding line profile fits are plotted in Figs. A.1–A.2. Both temperature maps show mostly cool spots at similar locations, accounting for the reliability of the image reconstruction. Indeed, most of the cool surface features appear on the combined Doppler map derived from all of the spectra (S1+S2); see Fig. 7.

The strongest feature, a cool, high latitude spot on the hemisphere of the visible pole of $\Delta T > -1000$ K temperature contrast relative to T_{eff} is shown on both S1 and S2 maps at around 0.45 phase, centered at $\beta \approx 50^\circ$. In addition, this large spot is getting more compact from S1 to S2. A mid-latitude spot is seen on the opposite (lower) hemisphere at ≈ 0.3 phase. Its location, however, is a bit shifted from S1 to S2 towards the invisible pole, or alternatively, its extension decreases. A weak cool spot is seen on S1 at ≈ 0.13 phase, elongated from 30° latitude down to the equator and even below to -30° . Such an elongated shape, however, may be the result of mirroring due to the high inclination. In deed, its antitype on S2 is less contrasted but more circular shaped and confined to the upper hemisphere, i.e., less mirrored. Another less contrasted cool spot is seen on S2 centered at 0.83

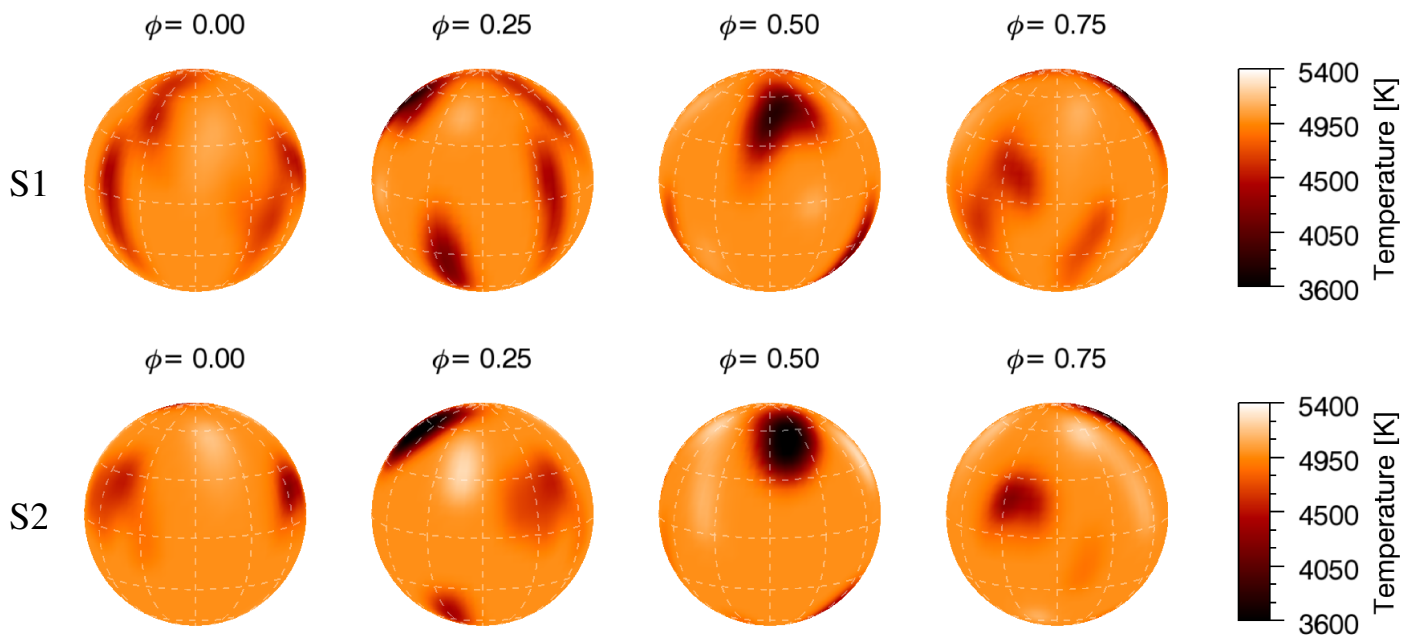


Fig. 6. Two Doppler images of V471 Tau from the 2005 data (S1 and S2). The surface temperature reconstructions are plotted in four rotational phases.

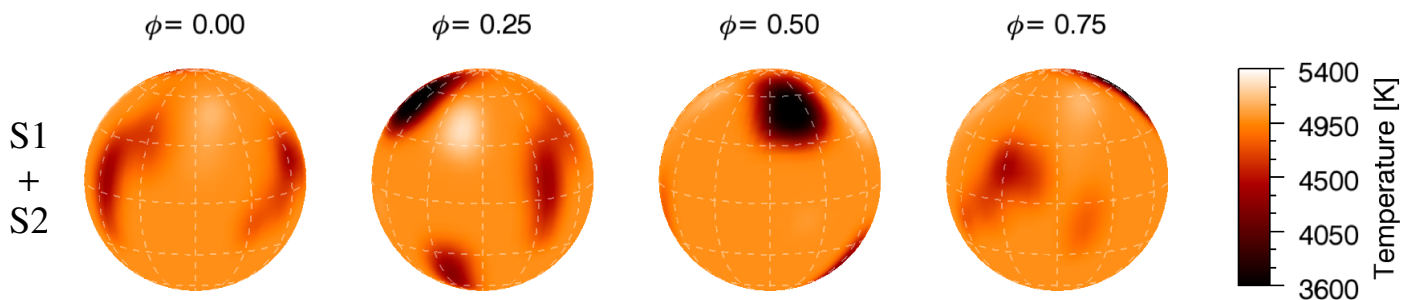


Fig. 7. Combined Doppler image of V471 Tau derived from all the available spectra from 2005 (S1+S2). The surface temperature map is plotted in four rotational phases.

phase and 20° latitude, which, again, has a weaker but more extended precursor on S1.

Some weak bright features are also seen, but their contrast hardly reaches $\Delta T \approx +200$ K and their location and shape are more changeful when comparing S1 image against S2. Their presence is even less salient on the average (S1+S2) image except the one at 0.3 phase. This feature, however, raises reliability issues. We know that spurious bright features can appear as an artifact of Doppler imaging coming from insufficient phase coverage (e.g. Lindborg et al. 2014). The phase coverages for both S1 and S2 were fairly good, the only remarkable phase gaps were between 0.288-0.500 and 0.171-0.318 in S1 and S2 datasets, respectively. This may explain the bright spot at 0.3 phase on the S2 reconstruction and account for some minor inconsistencies between S1 and S2 around these phase gaps. All in all, we think that those bright spots are mostly artifacts.

5.2.2. Doppler images from the 2014/15 CFHT spectra

Doppler images for the 2014/15 observing season (S3, S4) are presented in Fig. 8; for the corresponding line profile fits see

Figs. A.3-A.4. Again, the most dominant cool features in two subsequent maps appear at similar locations. However, neither the weaker cool features nor the bright features are particularly consistent. For example, bright features are more apparent in the S3 reconstruction, compared with S4. This is not surprising when keeping in mind that due to the unfavourable data distribution the selected spectra cover ≈ 20 days for S3 and ten days for S4. Moreover, the time gap between the mean HJDs of S3 and S4 is ≈ 15 days, therefore incoherences between the two images are more visible. The combined Doppler map derived from all of the spectra (S3+S4) in Fig. 9 indicates that the most coherent and most striking feature is the high latitude ($\beta \approx 55^\circ$) cool spot at around ≈ 0.4 phase, recalling the S1 and S2 reconstructions. This cool spot may be coupled to the orbital phase, as suggested in Schrijver & Zwaan (1991). We conclude that the weak and inconsistent features in the S3 and S4 reconstruction, being cool or bright, can either be the result of imperfections of the reconstruction or come from the unfavourable conditions of the data distribution.

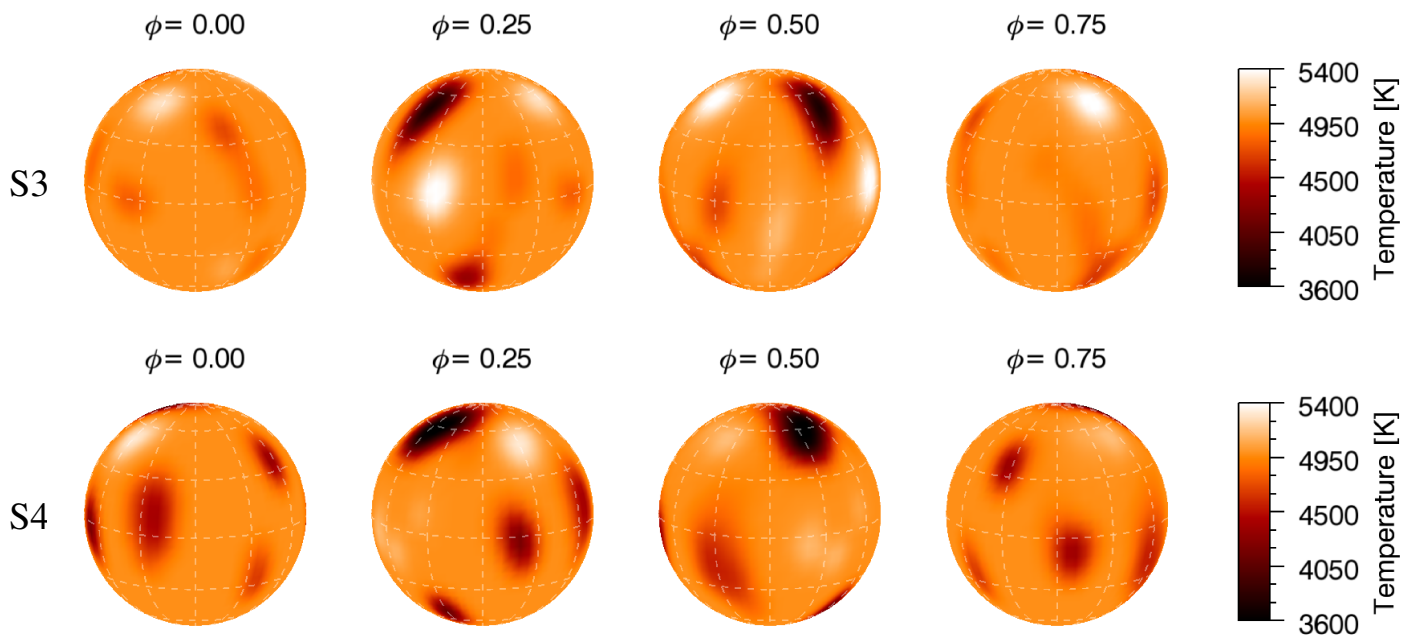


Fig. 8. Two Doppler images of V471 Tau for the second observing run at the turn 2014/2015 (S3 and S4). The surface temperature reconstructions are plotted in four rotational phases.

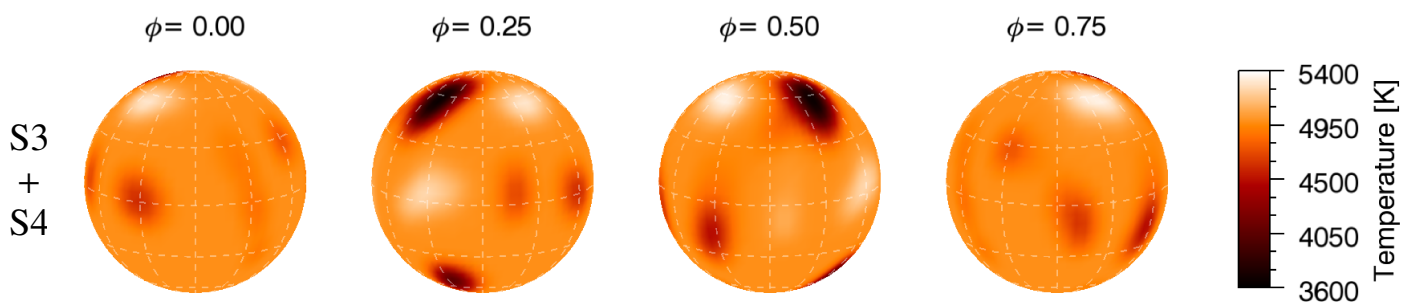


Fig. 9. Combined Doppler image of V471 Tau derived from all the spectra in the second observing run at the turn 2014/2015 (S3+S4). The surface temperature map is plotted in four rotational phases.

5.3. Differential rotation

Surface differential rotation can be measured by longitudinally cross-correlating consecutive Doppler images (Donati & Collier Cameron 1997; Kóvári et al. 2004), and fitting the latitudinal correlation peaks in the resulting cross-correlation function (ccf) map by a quadratic rotational law:

$$\Omega(\beta) = \Omega_{\text{eq}} - \Delta\Omega \sin^2 \beta, \quad (4)$$

where $\Omega(\beta)$ is the angular velocity at β latitude, Ω_{eq} is the angular velocity of the equator, and $\Delta\Omega = \Omega_{\text{eq}} - \Omega_{\text{pole}}$ gives the difference between the equatorial and polar angular velocities. With these, the dimensionless surface shear parameter α_{DR} is defined as $\alpha_{\text{DR}} = \Delta\Omega/\Omega_{\text{eq}}$, leading the following form:

$$\Omega(\beta) = \Omega_{\text{eq}}(1 - \alpha_{\text{DR}} \sin^2 \beta). \quad (5)$$

In our case two ccf maps can be composed, one for the two consecutive maps in the first observing season (S1, S2) and another one for the two maps in the second season (S3, S4). After the necessary normalization procedure the two ccf maps are combined to get an average ccf map (for the applied method

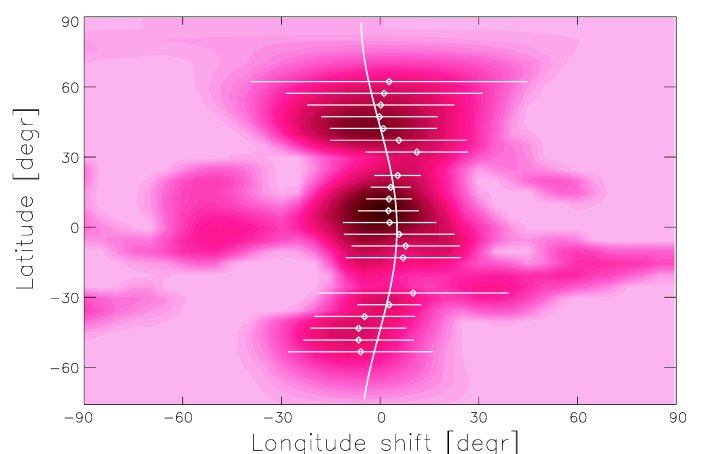


Fig. 10. Average cross-correlation function map derived from the subsequent Doppler images plotted in Fig.6 and Fig.8. Black represents strong correlation while light pink indicates no correlation. The quadratic sine fit (solid line) applied to the ridge of the correlation pattern (dots with error bars) suggests a solar-type rotational law with a very weak shear of $\alpha_{\text{DR}} = 0.0026 \pm 0.0006$. See Sect. 5.3 for details.

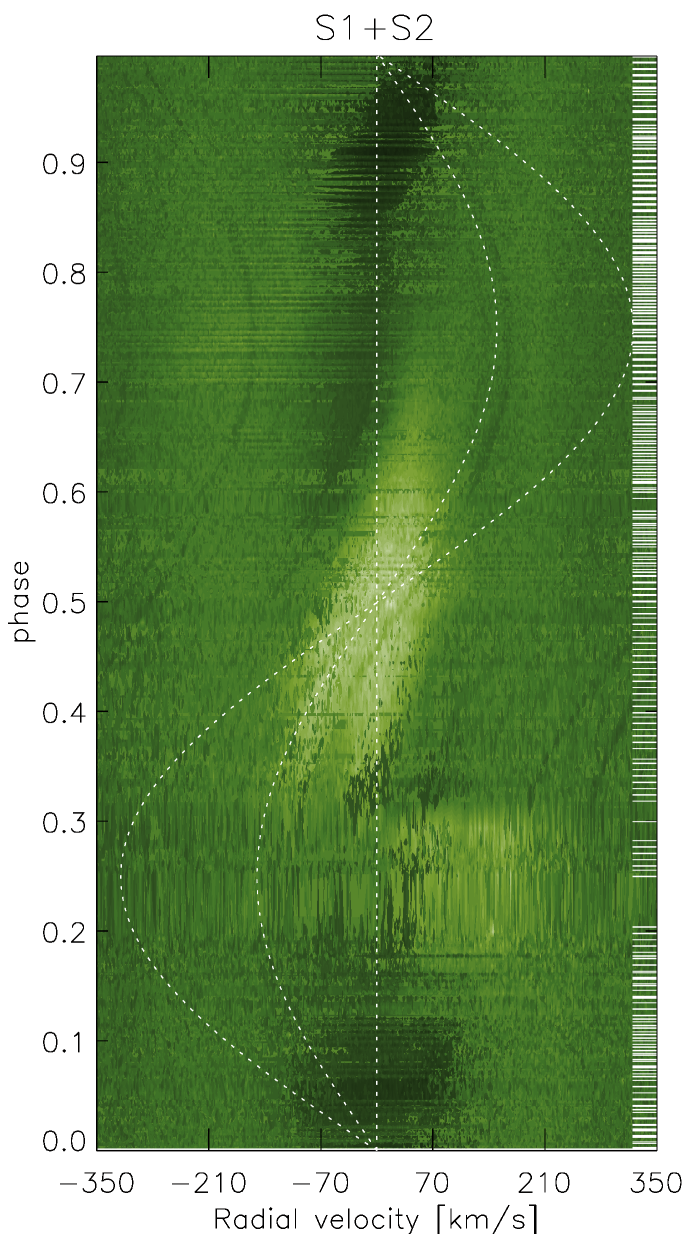


Fig. 11. Dynamic $H\alpha$ spectrum from the 2005 data (S1+S2). The individual 1-D $H\alpha$ spectra along the orbital phase are plotted in the rest frame of the K star. Dark green corresponds to deep absorption, while light yellow indicates strong emission. The large amplitude ($\approx 320 \text{ km s}^{-1}$) sine curve marks the radial velocity of the white dwarf, the smaller amplitude ($\approx 150 \text{ km s}^{-1}$) sinusoid is the radial velocity of the centre of mass of the binary system. Tick marks on the right indicate the phases of the observations.

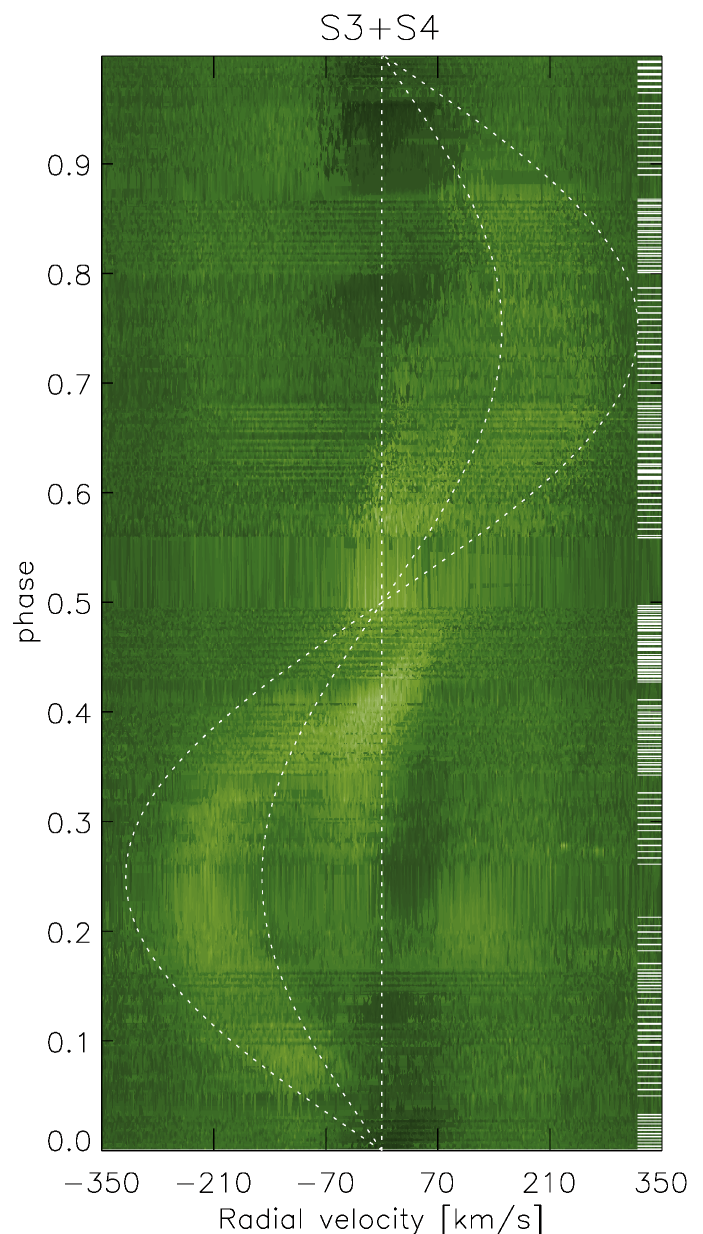


Fig. 12. Dynamic $H\alpha$ spectrum from the 2014/2015 data (S3+S4). Otherwise as in Fig. 11.

dubbed ACCORD see e.g., Kóvári et al. 2012, 2015). The correlation pattern in the ultimate average ccf map (Fig. 10) is fitted by a rotational law according to Eq. 5. The resulting fit indicates a very weak solar-type differential rotation, with $\Omega_{\text{eq}} = 691.57 \pm 0.13^\circ/\text{day}$ and $\alpha_{\text{DR}} = 0.0026 \pm 0.0006$ shear parameter, i.e., almost solid body rotation, in a fair agreement with the rough estimation from the K2 photometry (see Sect. 4.2). From the fitted Ω_{eq} and α_{DR} values we get $\beta_{\text{cor}} \approx 43^\circ$ for the co-rotating latitude, i.e., where rotation is synchronized exactly to the orbit.

6. Chromospheric and coronal activity

6.1. Variability of the $H\alpha$ line profile

$H\alpha$ line profile variation is capable to unfold chromospheric activity and presumably associated mass motions like CMEs. From the available time series of spectra we create time-slice plots for both observing runs. The resulting dynamic spectra are shown in Figs. 11-12. The plot for the first observing run (S1+S2) indicates absorption around 0.0 phase when the white dwarf is near or in eclipse. On the other hand, a strong emission develops between around 0.35-0.6. Clearly, the peaks of the absorption and the emission profiles stay within the $\pm 91 \text{ km s}^{-1}$ projected equatorial velocity range of the K star, suggesting that the sources are related to some surface features. Especially, the emission around the secondary eclipse may indicate relation with the dominant cool photospheric spot at around 0.45 phase (cf. Fig. 6). There may also be some extra emission on or over the receding side of

the K star between 0.2-0.3 phase, however, this part of the data has the lowest quality and even the phase coverage is not satisfactory, therefore we cannot make a definite statement about this feature.

The H α behaviour from the 2014/2015 data (S3+S4) in Fig. 12) shows similarities to the dynamic H α spectrum from the 2005 data, but quite different features are also present. Similar features are the absorption centered around 0.0 phase and the emission between 0.35-0.65 phase, this latter less conspicuous but still around the phase of the most prominent cool spot (see Fig. 8). Being within the radial velocity range of the K dwarf, it is very likely that these features are localized on the surface of the red dwarf. However, in addition to the similarities there is a very different emitting phenomenon located between the centre of mass of the system and the white dwarf. This emission is stronger in the first half of the orbital phase, but still visible during the second half. This suggests the presence of a clump of emitting plasma corotating with the system in the vicinity of the inner Lagrangian (L1) point, as already reported by Young et al. (1991). We note finally, that there may be some extra emission on the receding side of the K star around $\phi=0.2$, recalling Fig. 11, but the phase coverage is not satisfactory around and the emission peaks are not so strong, therefore, again, we could only guess about its reliability, nature and possible origin.

For further discussion about the peculiar emission from beyond the L1 point see Sect. 7.4.

6.2. X-ray emission from the K dwarf

The *ROSAT* pointed observations from 1991 were already analyzed by Wheatley (1998) who focused on the second, longer exposure that we also use here. The full wavelength coverage of the PSPC detector is 0.1-2.5 keV, i.e. the softer part is dominated by the emission from the white dwarf. Wheatley (1998) presented the light curve of the observation in a soft (0.1-0.4 keV) and a hard (0.4-1.2 keV) band. The soft band clearly shows the (partly covered) eclipse, which is not seen in the hard band, confirming that the harder X-ray emission stems from the K dwarf only. Both bands show variability, but no large flares. The *ROSAT* data are, however, affected by many data gaps due to the spacecraft orbit. Therefore, we simply use the average flux from this observation as the quasi-quiet state for this epoch. The 0.1-2.5 keV flux from the K dwarf only (determined by spectral modelling in Wheatley (1998)) amounts to $(4.0 \pm 0.2) \times 10^{-12} \text{ erg cm}^{-2} \text{ s}^{-1}$.

In 1996, V471 Tau was observed by *ASCA*. This observation is described and analyzed in detail by Still & Hussain (2003). Their light curve from the combined SIS and GIS data in the energy range 0.3-10 keV shows some variability which may be due to small flare events, but the number of potentially flaring data points is small compared to the full light curve. Still & Hussain (2003) used the whole observation for spectral modeling (due to the rather low count rate) and obtained an average flux of $2.4 \times 10^{-12} \text{ erg cm}^{-2} \text{ s}^{-1}$ valid for the 0.5-10 keV range, which we adopt here as well.

One year later, V471 Tau was observed with the *ROSAT* High Resolution Imager (HRI). This instrument has an energy range of 0.1-2.5 keV, but due to its negligible energy resolution the data cannot be binned in energy to remove the contribution from the white dwarf. Therefore, we extracted the light curve of the whole observation using the *xselect* task from the *HEASoft*¹ package. This observation covered a part of one eclipse. There-

fore, we used *xselect* to extract an image for the time interval of the eclipse only (thus containing only emission from the K dwarf) and determined the count rate with the *ximage/sosta* task, which performs also background subtraction and corrects for vignetting, deadtime, and PSF. Although the full light curve did not show any large flares, the short duration of the usable time interval makes this data point more uncertain.

The *Chandra* observations from 2002 were already analyzed in several studies (Drake & Sarna 2003; Ness et al. 2004; García-Alvarez et al. 2005). The HRC-S/LETG instrument provides high-resolution spectroscopy in the 0.07-7.29 keV range. The light curve shown by García-Alvarez et al. (2005) does not include any strong flares, so the average flux of the observation was adopted. This was taken from Ness et al. (2004) who extracted the flux in the smaller 5.15-38.19 Å wavelength band (quoted luminosity of $1.1234 \times 10^{30} \text{ erg s}^{-1}$), i.e. with negligible contribution from the white dwarf.

The first *XMM Newton* observation from 2004 was analyzed using the *XMM Newton* Scientific Analysis System (SAS) Version 17.0.0. We only use data from the EPIC/PN detector, as the simultaneous EPIC/MOS and RGS data have lower S/N ratio. The SAS task *epproc* was used to create an event list from the raw *odf* file for the EPIC/PN detector. We extracted source and background regions in *ds9* and use the SAS tasks *evselect* to create the light curves and *epiclccorr* to perform background subtraction and all necessary corrections (vignetting, deadtime, etc.). We use the energy band 0.3-10 keV to minimize potential contamination from the white dwarf at lower energies, and because we use this energy range for the common analysis of all instruments. This observation is affected by a large flare event previously analyzed by Pandey & Singh (2008) and significant variability. Therefore, we needed to use a restricted time range that most likely resembles a quasi-quiet state. We extract the last 18783 s of the observation which seems to be free of any trends, although there is still strong scatter in the light curve.

In 2015, V471 Tau was observed by *Swift*. We inspected the light curves from the XRT instrument created by the online tool of the *Swift* Science Center² (Evans et al. 2007, 2009). There are no strong flares in the data, so we simply adopt the averaged count rate from all observations in the 0.3-10 keV band.

The second *XMM Newton* observation from 2019 was processed an analyzed in the same way as described before. This observation was also affected by a large flare and strong variability, which required to extract the first 9381 s only, which seems to display a rather constant count rate without trends.

6.3. Evolution of the X-ray luminosity

To compare the X-ray emission from many different instruments requires to either convert the fluxes taken from the literature to a common energy range or to obtain the appropriate count-to-flux conversion factors for the different instruments. We use the tool *WebPIMMS*³ to perform the necessary conversions. This requires input of the Galactic hydrogen absorption and a spectral model for the source.

To constrain the plasma parameters of the K dwarf in V471 Tau we perform spectral modeling of the two *XMM Newton* data sets and *Swift*. For *XMM Newton*, we extract source and background spectra of the selected quasi-quiet time ranges using *evselect* and create the required *rmf* and *arf* files using

² https://www.swift.ac.uk/user_objects/

³ <https://heasarc.gsfc.nasa.gov/cgi-bin/Tools/w3pimms/w3pimms.pl>

¹ <https://heasarc.gsfc.nasa.gov/docs/software/heasoft/>

Table 4. Spectral fits to the quiescent parts of the two *XMM Newton* observations from 2004 and 2019 and the *Swift* data from 2015. Errors refer to the 90% confidence intervals returned by *Xspec*. The last column gives the goodness-of-fit and the degrees of freedom.

Data	kT_1 [eV]	EM_1 [10^{52} cm^{-3}]	kT_2 [eV]	EM_2 [10^{52} cm^{-3}]	Z [Z_\odot]	T_{av} [MK]	EM_{tot} [10^{52} cm^{-3}]	χ^2_{red} (DOF)
XMM 2004	$0.34^{+0.05}_{-0.02}$	$3.1^{+0.2}_{-0.2}$	$0.96^{+0.02}_{-0.02}$	$6.7^{+0.4}_{-0.4}$	$0.18^{+0.02}_{-0.02}$	8.86	9.9	1.503 (58)
XMM 2019	$0.36^{+0.04}_{-0.03}$	$2.6^{+0.3}_{-0.3}$	$1.01^{+0.02}_{-0.02}$	$6.0^{+0.4}_{-0.4}$	$0.18^{+0.02}_{-0.02}$	9.48	8.6	1.043 (58)
Swift 2015	$1.03^{+0.15}_{-0.08}$	$11.9^{+2.5}_{-2.3}$	–	–	$0.13^{+0.07}_{-0.05}$	–	–	0.999 ^a (132)

Notes. ^(a) Pearson χ^2_{red} due to use of Cash statistics for fitting.

rmfgen and *arfgen*. We use *specgroup* to group the files and select a minimum of 20 counts per bin and not oversampling the intrinsic energy resolution by more than a factor of three. We fit the spectra using *Xspec*⁴ with a model including Galactic absorption and a sum of APEC (Smith et al. 2001) plasma models. As the Galactic absorption is not very well constrained by a fit to energy ranges > 0.3 keV we fix the H column density towards V471 Tau to its measured value of $N_{\text{H}} = 1.62 \times 10^{18} \text{ cm}^{-2}$ (Wood et al. 2005). This has a negligible effect on the results, as this value is low because the star is nearby. For the fitting process, we restrict the energy range further to 0.3–3.9 keV due to low signal at higher energies. At both epochs, we find best fits with two APEC plasma components with the same coronal abundances (Table 4). The results are broadly consistent with each other, as well as other spectral analyses in the literature. We also tried to fit the *Swift* spectrum obtained from the online tool (Evans et al. 2009), but due to the small number of counts it was not possible to fit a 2-T plasma model. An acceptable fit was obtained for a 1-T model using Cash statistics (Cash 1979), yielding a temperature comparable to the hotter component of the more reliable *XMM Newton* fits and an emission measure similar to the total one obtained for *XMM Newton*. All fits predict subsolar coronal abundances ($Z \sim 0.2Z_\odot$), consistent with previous studies. Table 4 summarizes the plasma parameters obtained from the *Xspec* fits, together with the calculated average emission measure-weighted temperature T_{av} and total emission measure EM_{tot} for the 2-T fits.

As we do not find significant differences of coronal plasma parameters from the analyzed observations, we adopt a common parameter set for all flux conversions. For simplicity, we use a 1-T APEC model in *WebPIMMS* with a mean temperature of 8.9 MK ($\log T = 6.95$). We fix the Galactic N_{H} absorption to the value from Wood et al. (2005) and the coronal metal abundance to $0.2Z_\odot$. Using a 2-T model with parameters similar to those obtained in the *XMM-Newton* fits does not change the results significantly. To estimate uncertainties for the conversion factors, we run *WebPIMMS* with $\log T = 6.9$ and $\log T = 7.0$, corresponding to an uncertainty of the mean temperature by about 10%, which is slightly larger than what we calculate from the *XMM-Newton* spectra (3–4%). This results in uncertainties on the conversion factors by $\lesssim 3\%$.

After converting the fluxes taken from the literature and the count rates of the specific instruments to a common energy range of 0.3–10 keV, we use the distance from Table 2 to convert the fluxes to luminosities. The results are shown in Fig. 13. The displayed uncertainties on the X-ray luminosities include the statistical uncertainties of the flux/count rate measurements, the flux conversion factors, and the distance. The X-ray luminosity of the K dwarf shows variations over the years, with the maximum

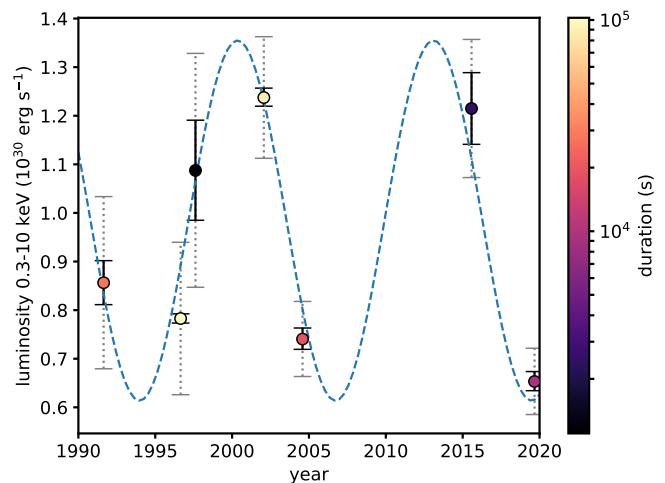


Fig. 13. Evolution of the X-ray luminosity of the K dwarf in V471 Tau from the observations summarized in Table 1. The duration of the selected quiescent ranges is color coded. Solid error bars denote flux errors (see text), dotted bars additionally the estimated cross-calibration uncertainty. The blue dashed line indicates the best fit with a sinusoidal function with a period of ~ 12.7 yr.

data point being 90% higher than the minimum one. As there are only seven data sets spanning almost 30 years, some with exposure times for the quasi-quiescent time intervals as short as ~ 20 min, a detailed investigation of a possible cycle is not feasible. Moreover, the data stem from a variety of different instruments and cross-calibration issues are expected to be present (see the detailed discussion in Wargelin et al. 2017). To account for such instrument cross-calibration uncertainties, we add 10% for *Chandra*, *XMM-Newton* and *Swift* data, as well as 20% for the older *ROSAT* and *ASCA* data to the luminosity uncertainties (Snowden 2002; Tsujimoto et al. 2011).

Despite the limitations of the available data, we fitted a sinusoidal function to the X-ray luminosities in Fig. 13. The blue dashed line in the plot corresponds to a period of about 12.7 yr, which can be interpreted as activity cycle. We stress again, however, that the uneven spacing of the observations, the small number of data points, as well as uncertainties of instrumental cross-calibration, do not allow a definitive conclusion about the existence of an X-ray cycle and its properties.

7. Discussions

7.1. Weak differential rotation and active longitude

From our Doppler reconstructions we have measured a very weak solar-type surface differential rotation for the K star

⁴ <https://heasarc.gsfc.nasa.gov/xanadu/xspec/>

(Sect. 5.3), Such a weak shear, however, is not surprising, as we essentially expect something similar for fast rotating late-type dwarf stars (see the empirical study by Kóvári et al. 2017, and their references). In addition, synchronization due to tidal dissipation in close binaries may suppress the rotational shear (Scharlemann 1982). In Hussain et al. (2006) authors reported almost rigid body rotation for V471 Tau with α_{DR} of 0.0001 ± 0.0005 shear coefficient. In comparison, our result of $\alpha_{DR} = 0.0026 \pm 0.0006$ is still weak, but an order of a magnitude stronger shear based on using much more data and our well-established cross-correlation technique ACCORD (for some applications and tests see, e.g. Kóvári et al. 2004, 2012, 2014, 2015, and their references). This technique amplifies independent cross-correlation signals from different epochs to multiply the credibility and reliability of the result. We note finally, that our larger shear coefficient is also supported by the short term photometric period changes (see Sect. 4.2).

The Doppler reconstructions performed in our study indicate that the most dominant surface spot located around 0.40-0.45 phase at $\beta \approx 50-55^\circ$ latitude may be a permanent feature (see Figs. 6-8). In the Doppler imaging study by Ramseyer et al. (1995) authors have found that a dominant cool spot appeared at the longitude facing the white dwarf in all their four Doppler maps (1992 September, October, December and 1993 December). Moreover, the Doppler image from 2002 November (Hussain et al. 2006) has also indicated that the most prominent spot was directed toward the white dwarf.

Asymmetric tidal distortion may significantly alter internal dynamos of rapidly rotating convective stars in close binaries (Rottler et al. 2002), which can result in an active longitude around the sub-white dwarf point in the K dwarf component. Such a non-axisymmetric nature of spot activity is not unusual in close binary systems (Oláh 2006). However, it has also been shown that the condition for the excitation of stable, non-axisymmetric fields is weak differential rotation (Scharlemann 1982; Ruediger & Elstner 1994), which we firmly confirmed in the case of V471 Tau.

7.2. Effective temperature rise around $\phi=0.5$ phase

The ≈ 100 K variation of the surface temperature of the K dwarf along the orbital phase (see Fig. 3) may be interpreted as the irradiation effect of the white dwarf. In fact, we have no means to calculate what fraction of the radiative energy from the white dwarf is converted to thermal reprocessing in the photosphere of the K star. However, according to Young et al. (1988, their Table 2) the estimated ratio of the total luminous energy intercepted from the white dwarf to the bolometric output of the K star is $\approx 0.6\%$, i.e., below the detection limit of 3% assumed for such a heating mechanism to be efficient in the photosphere. A similar conclusion has been drawn by O'Brien et al. (2001), who estimated that the luminosity of the K star would increase only by 1% due to the irradiation from the white dwarf, which would explain only ≈ 12 K temperature rise of the sub-white dwarf hemisphere. In contrast, the effective temperature change of ≈ 100 K in Fig. 3 would assume $\approx 8\%$ luminosity difference. At this point we speculate that the photospheric temperature rise around $\phi=0.5$ may rather be associated with increased magnetic activity at the sub-white dwarf hemisphere of the K star. It has been learned that faculae-dominated active stars tend to become brighter when their magnetic activity level increases (Radick et al. 1990). We believe that the hemispheric difference in magnetic activity observed in V471 Tau can have a significant effect on the overall hemispheric temperature difference as well

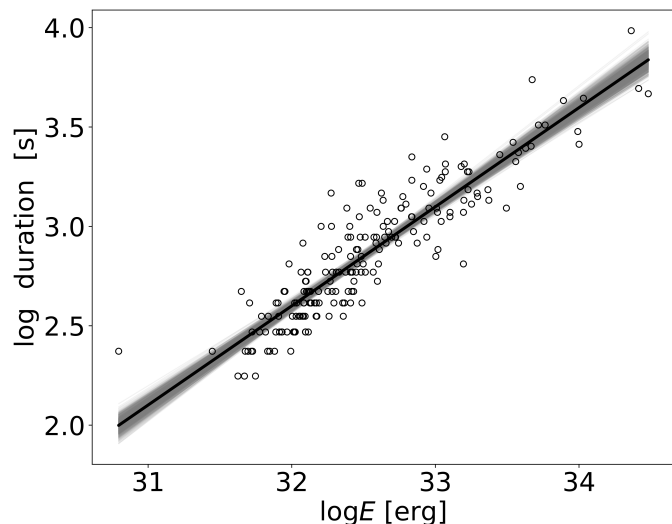


Fig. 14. Flare duration vs. flare energy from the *K2* data of V471 Tau. The best fit indicates a power-law relationship with 0.5 ± 0.02 index.

(cf. e.g. Gondoin 2008; Shapiro et al. 2016). That is, small-scale photospheric bright faculae, permanently present around the active longitude facing the white dwarf, may infer such a rise in the effective temperature.

7.3. Flare statistics

We find that the 198 flares detected in the 71-day long *K2* data of V471 Tau are distributed randomly over the rotational phase, i.e. no significant phase dependency was found in the flare occurrence. The derived flare energies in Sect. 4.3 range over four magnitudes. Recently, Kóvári et al. (2020) have concluded that, in principle, differences between flare energies are due to size effect, regardless of energy range or spectral type (cf. Balona 2015). Accordingly, flare duration is supposed to increase with flare energy. In Fig. 14 we plot $\log \Delta t$ flare duration as a function of $\log E_f$ flare energy. The relationship on the log-log plot fitted by a linear function yields a 0.50 ± 0.02 slope. In comparison, Maehara et al. (2015) suggested a generalized function between flare duration and flare energy with a power-law index (slope) of $\approx 1/3$.

It has been suggested (see e.g. Parker 1988; Hudson 1991; Saar & Bookbinder 1998) that the more numerous small flaring events have an important role in heating the plasma in the transition region and the corona. This is supported by the power-law index of $\alpha \gtrsim 2.0$ derived from flare statistics of magnetically active M dwarf stars (e.g., Ilin et al. 2019, etc.). In comparison, $\alpha = 1.7$ was obtained for 27 young K 5-7 stars in the Orion Nebula Cluster (Wolk et al. 2005). However, no such a difference was found from the flare statistics for 548 M and 343 K dwarf stars ($\alpha = 1.82$ and 1.86, respectively) in Lin et al. (2019). Nevertheless, the α index of 1.8 obtained for V471 Tau (see Fig. 5) suggests that the dissipating energy of the flares should have a significant contribution in heating the upper atmosphere.

7.4. Inter-binary $H\alpha$ emission during activity maximum

The cycle period of the sinusoid fitted to the X-ray luminosity variation in Fig. 13 is comparable to the 13 yr period identified in timing residuals by Vaccaro et al. (2015) and a possible ≈ 10 yr periodicity from an activity cycle mentioned by Kamiński

et al. (2007). Moreover, Kamiński et al. (2007) stated that during observations with *MOST* in Dec 2005 the star was much less spotted than in the previous observations of Hussain et al. (2006) (from Nov 2002) and had only little photometric variability, which the authors interpreted as the evidence that the K dwarf was close to an activity minimum. This is consistent with our fit to the X-ray data.

According to Fig. 13, about four months ahead of the epochs of the S1-S2 Doppler reconstructions, in 2004 the X-ray luminosity of V471 Tau was around its minimum. While about six months after the epochs of the S3-S4 Doppler images, in 2015 the X-ray luminosity was much higher, according to the data point from *Swift*. Oddly, such a large difference is not seen when comparing the overall spottedness in the S1-S2 images with that of S3-S4, which are quite similar, despite the ≈ 9 -year time gap between them. However, the $H\alpha$ line profile variability (see Figs. 11-12) showed indeed different behaviour in the two observing runs. The extra $H\alpha$ emission from the inter-binary space (see Fig. 12) might have something to do with the enhanced X-ray luminosity in 2015, i.e., around activity maximum. In deed, this is supported by the result in Young et al. (1991, see their Fig. 3) who also found external $H\alpha$ emission component, originated from somewhere in the inter-binary space beyond the centre of mass of the system, expanding towards the white dwarf, definitely reminiscent of our result plotted in Fig. 12. Moreover, their observations were obtained in Nov 3-4, 1988 and Jan 29-30, 1989, i.e., close to the suspected maximum of the activity cycle ended in 1994 (according to our Fig. 13). As a further support see also Rottler et al. (2002) for the secular $H\alpha$ variability in 1985, 1990 and 1992.

We expect that during the magnetic cycle, around activity maximum more and/or more extended magnetic loops develop high above the surface, reaching one stellar radius (Guinan et al. 1986), and this way more cool material enters the upper atmosphere in trapped clumps, similar to solar prominences. Large prominence-like condensations of cool material were reported from $H\alpha$ observations of AB Dor Collier Cameron & Robinson (1989), a single K0 dwarf, rotating as rapidly as V471 Tau. Normally, such a clump of cool material appears in absorption in $H\alpha$, exactly what we actually see on the far side of the K star around zero phase. However, it can get into emission when heated due to the UV radiation from the white dwarf. The physical process behind heating proposed first by Young et al. (1988) involves fluorescence-induced $H\alpha$ emission (see also Bois et al. 1991). This scenario could explain the $H\alpha$ line variability both around the activity minimum (Fig. 11) when there are no extended magnetic loops, and around maximum (Fig. 12) when extended loops with cool material trapped in them are present. Still, we caution that our ground-based spectroscopic data and the space observations did not overlap exactly and the available space data is limited. Therefore our conclusion about such a link between the peculiar $H\alpha$ emission from the vicinity of the L1 point and the proximity of the activity cycle maximum may raise some criticism.

8. Conclusions

We confirm that the magnetic activity of the K dwarf component in V471 Tau is strongly influenced by the close white dwarf companion. Our related concluding remarks are as follows:

- We confirm that there is a permanent active longitude on the K star facing the white dwarf over decades, regardless of the actual phase of the magnetic cycle.

- We confirm a weak solar-type surface differential rotation on the surface of the K star, supporting theoretical expectations.
- We suggest that frequent flaring should have a significant contribution in heating the corona of the K star.
- From the long-term evolution of X-ray luminosity we confirm a magnetic activity cycle of ≈ 12.7 ys, whose traces appear also in the chromospheric ($H\alpha$) activity pattern.
- We find that the inter-binary $H\alpha$ emission from the vicinity of the L1 point is correlated with the activity cycle: it intensifies during activity maximum and fades away during minimum.

Acknowledgements. This publication makes use of VOSA, developed under the Spanish Virtual Observatory project supported by the Spanish MINECO through grant AyA2017-84089. VOSA has been partially updated by using funding from the European Union's Horizon 2020 Research and Innovation Programme, under Grant Agreement No. 776403 (EXOPLANETS-A). This work was supported by the Hungarian National Research, Development and Innovation Office grant OTKA K131508, KH-130526, by the Lendület Program of the Hungarian Academy of Sciences, project No. LP2018-7/2019 and by the NKFIH grant 2019-2.1.11-TÉT-2019-00056. Authors acknowledge the financial support of the Austrian-Hungarian Action Foundation (98őu5, 101őu13). TB acknowledges the financial support of the Hungarian National Research, Development and Innovation Office grant NKFIH KH-130372. LK acknowledges the financial support of the Hungarian National Research, Development and Innovation Office grant NKFIH PD-134784.

References

- Adibekyan, V. Z., Delgado Mena, E., Sousa, S. G., et al. 2012, *A&A*, 547, A36
- Balona, L. A. 2015, *MNRAS*, 447, 2714
- Barstow, M. A., Schmitt, J. H. M. M., Clemens, J. C., et al. 1992, *MNRAS*, 255, 369
- Bayo, A., Rodrigo, C., Barrado Y Navascués, D., et al. 2008, *A&A*, 492, 277
- Bois, B., Lanning, H. H., & Mochnacki, S. W. 1991, *AJ*, 102, 2079
- Bond, H. E., Mullan, D. J., O'Brien, M. S., & Sion, E. M. 2001, *ApJ*, 560, 919
- Borkovits, T., Rappaport, S. A., Hajdu, T., et al. 2020, *MNRAS*, 493, 5005
- Carroll, T. A., Kopf, M., & Strassmeier, K. G. 2008, *A&A*, 488, 781
- Carroll, T. A., Strassmeier, K. G., Rice, J. B., & Künstler, A. 2012, *A&A*, 548, A95
- Cash, W. 1979, *ApJ*, 228, 939
- Castelli, F. & Kurucz, R. L. 2004, *ArXiv Astrophysics e-prints* [astro-ph/0405087]
- Collier Cameron, A. & Robinson, R. D. 1989, *MNRAS*, 238, 657
- Csúbrly, Z. & Kolláth, Z. 2004, in *ESA Special Publication*, Vol. 559, SOHO 14 Helio- and Asteroseismology: Towards a Golden Future, ed. D. Danesy, 396
- Cully, S. L., Dupuis, J., Rodríguez-Bell, T., et al. 1996, in *IAU Colloq.* 152: Astrophysics in the Extreme Ultraviolet, ed. S. Bowyer & R. F. Malina, 349
- Donati, J.-F. & Collier Cameron, A. 1997, *MNRAS*, 291, 1
- Drake, J. J. & Sarna, M. J. 2003, *ApJ*, 594, L55
- Evans, P. A., Beardmore, A. P., Page, K. L., et al. 2009, *MNRAS*, 397, 1177
- Evans, P. A., Beardmore, A. P., Page, K. L., et al. 2007, *A&A*, 469, 379
- Evren, S., Ibanoglu, C., Tunca, Z., & Tumer, O. 1986, *Ap&SS*, 120, 97
- Flower, P. J. 1996, *ApJ*, 469, 355
- Gaia Collaboration, Brown, A. G. A., Vallenari, A., et al. 2018, *A&A*, 616, A1
- García-Alvarez, D., Drake, J. J., Lin, L., Kashyap, V. L., & Ball, B. 2005, *ApJ*, 621, 1009
- Gershberg, R. E. 1972, *Ap&SS*, 19, 75
- Gondoin, P. 2008, *A&A*, 478, 883
- Gossage, S., Conroy, C., Dotter, A., et al. 2018, *ApJ*, 863, 67
- Guinan, E. F. & Ribas, I. 2001, *ApJ*, 546, L43
- Guinan, E. F. & Sion, E. M. 1984, *AJ*, 89, 1252
- Guinan, E. F., Wacker, S. W., Baliunas, S. L., Loesser, J. G., & Raymond, J. C. 1986, in *ESA Special Publication*, Vol. 263, *New Insights in Astrophysics. Eight Years of UV Astronomy with IUE*, ed. E. J. Rolfe & R. Wilson, 197–200
- Gustafsson, B., Edvardsson, B., Eriksson, K., et al. 2008, *A&A*, 486, 951
- Hardy, A., Schreiber, M. R., Parsons, S. G., et al. 2015, *ApJ*, 800, L24
- Hawley, S. L., Davenport, J. R. A., Kowalski, A. F., et al. 2014, *ApJ*, 797, 121
- Hill, C. A., Watson, C. A., Shahbaz, T., Steeghs, D., & Dhillion, V. S. 2014, *MNRAS*, 444, 192
- Howell, S. B., Sobek, C., Haas, M., et al. 2014, *PASP*, 126, 398
- Hudson, H. S. 1991, *Sol. Phys.*, 133, 357
- Hussain, G. A. J., Allende Prieto, C., Saar, S. H., & Still, M. 2006, *MNRAS*, 367, 1699

- İbanoğlu, C., Evren, S., Taş, G., & Çakırh, Ö. 2005, MNRAS, 360, 1077
- Ilin, E., Schmidt, S. J., Davenport, J. R. A., & Strassmeier, K. G. 2019, A&A, 622, A133
- Jensen, K. A., Swank, J. H., Petre, R., et al. 1986, ApJ, 309, L27
- Kamiński, K. Z., Ruciński, S. M., Matthews, J. M., et al. 2007, AJ, 134, 1206
- Kóvári, Zs., Bartus, J., Kriskovics, L., Vida, K., & Oláh, K. 2014, in *Magnetic Fields throughout Stellar Evolution*, ed. P. Petit, M. Jardine, & H. C. Spruit, Vol. 302, 198–199
- Kóvári, Zs., Korhonen, H., Kriskovics, L., et al. 2012, A&A, 539, A50
- Kóvári, Zs., Kriskovics, L., Künstler, A., et al. 2015, A&A, 573, A98
- Kóvári, Zs., Oláh, K., Günther, M. N., et al. 2020, A&A, 641, A83
- Kóvári, Zs., Oláh, K., Kriskovics, L., et al. 2017, *Astronomische Nachrichten*, 338, 903
- Kóvári, Zs., Strassmeier, K. G., Granzer, T., et al. 2004, A&A, 417, 1047
- Kriskovics, L., Kóvári, Zs., Vida, K., et al. 2019, A&A, 627, A52
- Kupka, F., Piskunov, N., Ryabchikova, T. A., Stempels, H. C., & Weiss, W. W. 1999, A&AS, 138, 119
- Lanza, A. F. 2020, MNRAS, 491, 1820
- Lin, C. L., Ip, W. H., Hou, W. C., Huang, L. C., & Chang, H. Y. 2019, ApJ, 873, 97
- Lindborg, M., Hackman, T., Mantere, M. J., et al. 2014, A&A, 562, A139
- Maehara, H., Shibayama, T., Notsu, Y., et al. 2015, *Earth, Planets, and Space*, 67, 59
- Ness, J. U., Güdel, M., Schmitt, J. H. M. M., Audard, M., & Telleschi, A. 2004, A&A, 427, 667
- Notsu, Y., Maehara, H., Honda, S., et al. 2019, ApJ, 876, 58
- O'Brien, M. S., Bond, H. E., & Sion, E. M. 2001, ApJ, 563, 971
- Oláh, K. 2006, Ap&SS, 304, 145
- Pandey, J. C. & Singh, K. P. 2008, MNRAS, 387, 1627
- Parker, E. N. 1988, ApJ, 330, 474
- Piskunov, N. & Valenti, J. A. 2017, A&A, 597, A16
- Radick, R. R., Lockwood, G. W., & Baliunas, S. L. 1990, *Science*, 247, 39
- Ramseyer, T. F., Hatzes, A. P., & Jablonski, F. 1995, AJ, 110, 1364
- Rottler, L., Batalha, C., Young, A., & Vogt, S. 2002, A&A, 392, 535
- Rucinski, S. M. 1981, *Acta Astron.*, 31, 37
- Ruediger, G. & Elstner, D. 1994, A&A, 281, 46
- Saar, S. H. & Bookbinder, J. A. 1998, in *Astronomical Society of the Pacific Conference Series*, Vol. 154, *Cool Stars, Stellar Systems, and the Sun*, ed. R. A. Donahue & J. A. Bookbinder, 1560
- Scharlemann, E. T. 1982, ApJ, 253, 298
- Schrijver, C. J. & Zwaan, C. 1991, A&A, 251, 183
- Shapiro, A. I., Solanki, S. K., Krivova, N. A., Yeo, K. L., & Schmutz, W. K. 2016, A&A, 589, A46
- Smith, R. K., Brickhouse, N. S., Liedahl, D. A., & Raymond, J. C. 2001, ApJ, 556, L91
- Snowden, S. L. 2002, arXiv e-prints, astro
- Still, M. & Hussain, G. 2003, ApJ, 597, 1059
- Taylor, B. J. 2006, AJ, 132, 2453
- Tsujimoto, M., Guainazzi, M., Plucinsky, P. P., et al. 2011, A&A, 525, A25
- Vaccaro, T. R., Wilson, R. E., Van Hamme, W., & Terrell, D. 2015, ApJ, 810, 157
- Valenti, J. A. & Fischer, D. A. 2005, ApJS, 159, 141
- Vida, K. & Roettenbacher, R. M. 2018, A&A, 616, A163
- Wargelin, B. J., Saar, S. H., Pojmański, G., Drake, J. J., & Kashyap, V. L. 2017, MNRAS, 464, 3281
- Wheatley, P. J. 1998, MNRAS, 297, 1145
- Wilson, R. E. 1953, *Carnegie Institute Washington D.C. Publication*, 0
- Wolk, S. J., Harnden, F. R., J., Flaccomio, E., et al. 2005, ApJS, 160, 423
- Wood, B. E., Redfield, S., Linsky, J. L., Müller, H.-R., & Zank, G. P. 2005, ApJS, 159, 118
- Young, A., Klimke, A., Africano, J. L., et al. 1983, ApJ, 267, 655
- Young, A., Rottler, L., & Skumanich, A. 1991, ApJ, 378, L25
- Young, A., Skumanich, A., & Paylor, V. 1988, ApJ, 334, 397

Appendix A: Log of spectroscopic data

Table A.1. List of ESPaDOnS spectra of V471 Tau taken from the CFHT Science Archive. Given are the Heliocentric Julian Dates (HJD–2 450 000), dates (dd.mm.yyyy), rotational phases computed using Eq. 1, signal-to-noise ratios (S/N) for the four subsets (S1–S4) formed for Doppler imaging.

HJD	Date	Phase	S/N	Subset
3718.714	14.12.2005	0.703	60	S1
3718.717	14.12.2005	0.709	58	S1
3718.720	14.12.2005	0.714	62	S1
3718.723	14.12.2005	0.720	65	S1
3718.728	14.12.2005	0.730	62	S1
3718.731	14.12.2005	0.735	64	S1
3718.734	14.12.2005	0.741	63	S1
3718.736	14.12.2005	0.745	63	S1
3718.740	14.12.2005	0.753	63	S1
3718.742	14.12.2005	0.757	64	S1
3718.745	14.12.2005	0.762	66	S1
3718.748	14.12.2005	0.768	68	S1
3718.751	14.12.2005	0.774	66	S1
3718.754	14.12.2005	0.780	65	S1
3718.757	14.12.2005	0.785	63	S1
3718.760	14.12.2005	0.791	63	S1
3718.763	14.12.2005	0.797	64	S1
3718.766	14.12.2005	0.803	65	S1
3718.769	14.12.2005	0.808	64	S1
3718.772	14.12.2005	0.814	58	S1
3718.776	14.12.2005	0.822	50	S1
3718.779	14.12.2005	0.828	49	S1
3718.782	14.12.2005	0.833	43	S1
3718.785	14.12.2005	0.839	43	S1
3718.788	14.12.2005	0.845	49	S1
3718.791	14.12.2005	0.851	50	S1
3718.794	14.12.2005	0.856	52	S1
3718.797	14.12.2005	0.862	59	S1
3718.800	14.12.2005	0.868	64	S1
3718.803	14.12.2005	0.874	64	S1
3718.806	14.12.2005	0.879	61	S1
3718.808	14.12.2005	0.883	61	S1
3718.811	14.12.2005	0.889	58	S1
3718.814	14.12.2005	0.895	62	S1
3718.817	14.12.2005	0.900	60	S1
3718.820	14.12.2005	0.906	57	S1
3718.825	14.12.2005	0.916	60	S1
3718.828	14.12.2005	0.922	61	S1
3718.831	14.12.2005	0.927	54	S1
3718.833	14.12.2005	0.931	58	S1
3718.837	14.12.2005	0.939	49	S1
3718.849	14.12.2005	0.962	60	S1
3718.852	14.12.2005	0.968	60	S1
3718.855	14.12.2005	0.973	53	S1
3718.858	14.12.2005	0.979	58	S1
3718.861	14.12.2005	0.985	50	S1
3718.864	14.12.2005	0.991	51	S1
3718.867	14.12.2005	0.996	52	S1
3718.870	14.12.2005	0.002	57	S1
3718.873	14.12.2005	0.008	58	S1
3718.876	14.12.2005	0.014	57	S1

HJD	Date	Phase	S/N	Subset
3718.879	14.12.2005	0.019	56	S1
3718.881	14.12.2005	0.023	57	S1
3718.884	14.12.2005	0.029	53	S1
3718.887	14.12.2005	0.035	50	S1
3718.890	14.12.2005	0.041	52	S1
3718.893	14.12.2005	0.046	53	S1
3718.904	14.12.2005	0.067	51	S1
3718.907	14.12.2005	0.073	59	S1
3718.909	14.12.2005	0.077	60	S1
3718.912	14.12.2005	0.083	59	S1
3718.915	14.12.2005	0.088	59	S1
3718.918	14.12.2005	0.094	61	S1
3718.921	14.12.2005	0.100	60	S1
3718.924	14.12.2005	0.106	57	S1
3718.927	14.12.2005	0.112	54	S1
3718.930	14.12.2005	0.117	56	S1
3718.933	14.12.2005	0.123	53	S1
3718.936	14.12.2005	0.129	52	S1
3718.939	14.12.2005	0.135	51	S1
3718.942	14.12.2005	0.140	57	S1
3718.945	14.12.2005	0.146	54	S1
3718.948	14.12.2005	0.152	56	S1
3718.951	14.12.2005	0.158	45	S1
3718.954	14.12.2005	0.163	52	S1
3718.957	14.12.2005	0.169	51	S1
3718.960	14.12.2005	0.175	53	S1
3718.963	14.12.2005	0.181	48	S1
3718.966	14.12.2005	0.186	41	S1
3718.969	14.12.2005	0.192	45	S1
3718.972	14.12.2005	0.198	48	S1
3718.975	14.12.2005	0.204	49	S1
3718.999	14.12.2005	0.250	43	S1
3719.002	14.12.2005	0.255	40	S1
3719.004	14.12.2005	0.259	43	S1
3719.007	14.12.2005	0.265	52	S1
3719.010	14.12.2005	0.271	46	S1
3719.013	14.12.2005	0.277	45	S1
3719.016	14.12.2005	0.282	46	S1
3719.019	14.12.2005	0.288	42	S1
3720.693	16.12.2005	0.500	56	S1
3720.696	16.12.2005	0.506	59	S1
3720.699	16.12.2005	0.511	63	S1
3720.702	16.12.2005	0.517	64	S1
3720.705	16.12.2005	0.523	64	S1
3720.707	16.12.2005	0.527	70	S1
3720.710	16.12.2005	0.533	68	S1
3720.713	16.12.2005	0.538	69	S1
3720.716	16.12.2005	0.544	69	S1
3720.719	16.12.2005	0.550	70	S1
3720.722	16.12.2005	0.556	68	S1
3720.725	16.12.2005	0.561	69	S1
3720.728	16.12.2005	0.567	73	S1
3720.730	16.12.2005	0.571	73	S1
3720.733	16.12.2005	0.577	71	S1
3720.736	16.12.2005	0.582	71	S1
3720.742	16.12.2005	0.594	71	S1
3720.745	16.12.2005	0.600	72	S1
3720.747	16.12.2005	0.604	72	S1
3720.750	16.12.2005	0.609	74	S1
3720.753	16.12.2005	0.615	74	S1
3720.756	16.12.2005	0.621	75	S1

HJD	Date	Phase	S/N	Subset	HJD	Date	Phase	S/N	Subset
3720.759	16.12.2005	0.627	74	S1	3720.943	16.12.2005	0.980	68	S2
3720.762	16.12.2005	0.632	74	S1	3720.946	16.12.2005	0.985	66	S2
3720.765	16.12.2005	0.638	76	S1	3720.949	16.12.2005	0.991	65	S2
3720.768	16.12.2005	0.644	76	S1	3720.952	16.12.2005	0.997	62	S2
3720.771	16.12.2005	0.650	76	S1	3720.955	16.12.2005	0.003	63	S2
3720.774	16.12.2005	0.655	76	S1	3720.957	16.12.2005	0.006	62	S2
3720.777	16.12.2005	0.661	76	S1	3720.960	16.12.2005	0.012	60	S2
3720.779	16.12.2005	0.665	76	S1	3720.963	16.12.2005	0.018	61	S2
3720.782	16.12.2005	0.671	77	S1	3720.966	16.12.2005	0.024	61	S2
3720.785	16.12.2005	0.676	77	S1	3720.969	16.12.2005	0.030	63	S2
3720.790	16.12.2005	0.686	78	S1	3720.973	16.12.2005	0.037	64	S2
3720.793	16.12.2005	0.692	78	S1	3720.975	16.12.2005	0.041	60	S2
3720.796	16.12.2005	0.698	77	S1	3720.978	16.12.2005	0.047	62	S2
3720.799	16.12.2005	0.703	77	S1	3720.981	16.12.2005	0.053	60	S2
3720.802	16.12.2005	0.709	78	S1	3720.984	16.12.2005	0.058	63	S2
3720.805	16.12.2005	0.715	78	S1	3720.987	16.12.2005	0.064	60	S2
3720.808	16.12.2005	0.721	80	S1	3720.990	16.12.2005	0.070	60	S2
3720.811	16.12.2005	0.726	80	S1	3720.993	16.12.2005	0.076	62	S2
3720.814	16.12.2005	0.732	79	S1	3720.996	16.12.2005	0.081	61	S2
3720.816	16.12.2005	0.736	79	S1	3720.999	16.12.2005	0.087	59	S2
3720.819	16.12.2005	0.742	78	S1	3721.001	16.12.2005	0.091	57	S2
3720.822	16.12.2005	0.747	78	S1	3721.004	16.12.2005	0.097	58	S2
3720.825	16.12.2005	0.753	55	S1	3721.007	16.12.2005	0.102	57	S2
3720.830	16.12.2005	0.763	77	S1	3721.010	16.12.2005	0.108	53	S2
3720.833	16.12.2005	0.769	79	S1	3721.013	16.12.2005	0.114	54	S2
3720.836	16.12.2005	0.774	79	S1	3721.016	16.12.2005	0.120	52	S2
3720.839	16.12.2005	0.780	80	S1	3721.026	16.12.2005	0.139	53	S2
3720.842	16.12.2005	0.786	79	S1	3721.032	16.12.2005	0.150	55	S2
3720.845	16.12.2005	0.792	77	S1	3721.035	16.12.2005	0.156	53	S2
3720.848	16.12.2005	0.797	75	S1	3721.038	16.12.2005	0.162	53	S2
3720.851	16.12.2005	0.803	74	S1	3721.046	16.12.2005	0.177	48	S2
3720.854	16.12.2005	0.809	74	S1	3722.683	18.12.2005	0.318	60	S2
3720.856	16.12.2005	0.813	72	S1	3722.686	18.12.2005	0.324	63	S2
3720.859	16.12.2005	0.818	70	S1	3722.689	18.12.2005	0.330	62	S2
3720.862	16.12.2005	0.824	70	S1	3722.692	18.12.2005	0.335	62	S2
3720.865	16.12.2005	0.830	71	S1	3722.695	18.12.2005	0.341	66	S2
3720.868	16.12.2005	0.836	71	S2	3722.698	18.12.2005	0.347	66	S2
3720.871	16.12.2005	0.841	71	S2	3722.701	18.12.2005	0.353	68	S2
3720.874	16.12.2005	0.847	72	S2	3722.703	18.12.2005	0.357	68	S2
3720.879	16.12.2005	0.857	70	S2	3722.708	18.12.2005	0.366	71	S2
3720.882	16.12.2005	0.863	69	S2	3722.711	18.12.2005	0.372	70	S2
3720.884	16.12.2005	0.866	69	S2	3722.714	18.12.2005	0.378	69	S2
3720.887	16.12.2005	0.872	68	S2	3722.717	18.12.2005	0.383	69	S2
3720.890	16.12.2005	0.878	66	S2	3722.720	18.12.2005	0.389	73	S2
3720.893	16.12.2005	0.884	66	S2	3722.723	18.12.2005	0.395	73	S2
3720.896	16.12.2005	0.889	65	S2	3722.725	18.12.2005	0.399	74	S2
3720.899	16.12.2005	0.895	66	S2	3722.728	18.12.2005	0.405	77	S2
3720.902	16.12.2005	0.901	64	S2	3722.731	18.12.2005	0.410	78	S2
3720.905	16.12.2005	0.907	63	S2	3722.734	18.12.2005	0.416	77	S2
3720.908	16.12.2005	0.912	64	S2	3722.737	18.12.2005	0.422	77	S2
3720.911	16.12.2005	0.918	63	S2	3722.740	18.12.2005	0.428	80	S2
3720.914	16.12.2005	0.924	64	S2	3722.743	18.12.2005	0.433	80	S2
3720.916	16.12.2005	0.928	64	S2	3722.746	18.12.2005	0.439	79	S2
3720.919	16.12.2005	0.934	64	S2	3722.749	18.12.2005	0.445	78	S2
3720.922	16.12.2005	0.939	67	S2	3722.752	18.12.2005	0.451	77	S2
3720.926	16.12.2005	0.947	66	S2	3722.755	18.12.2005	0.456	77	S2
3720.928	16.12.2005	0.951	63	S2	3722.758	18.12.2005	0.462	75	S2
3720.931	16.12.2005	0.957	62	S2	3722.761	18.12.2005	0.468	75	S2
3720.934	16.12.2005	0.962	65	S2	3722.764	18.12.2005	0.474	75	S2
3720.937	16.12.2005	0.968	68	S2	3722.767	18.12.2005	0.479	75	S2
3720.940	16.12.2005	0.974	69	S2	3722.770	18.12.2005	0.485	75	S2

HJD	Date	Phase	S/N	Subset	HJD	Date	Phase	S/N	Subset
3722.772	18.12.2005	0.489	74	S2	3722.966	18.12.2005	0.861	74	S2
3722.775	18.12.2005	0.495	75	S2	3722.969	18.12.2005	0.867	73	S2
3722.778	18.12.2005	0.500	76	S2	3722.972	18.12.2005	0.873	75	S2
3722.781	18.12.2005	0.506	75	S2	3722.975	18.12.2005	0.878	75	S2
3722.784	18.12.2005	0.512	76	S2	3722.978	18.12.2005	0.884	74	S2
3722.787	18.12.2005	0.518	76	S2	3722.981	18.12.2005	0.890	74	S2
3722.790	18.12.2005	0.523	75	S2	3722.984	18.12.2005	0.896	74	S2
3722.793	18.12.2005	0.529	73	S2	3722.987	18.12.2005	0.901	75	S2
3722.796	18.12.2005	0.535	68	S2	3722.990	18.12.2005	0.907	75	S2
3722.799	18.12.2005	0.541	64	S2	3722.993	18.12.2005	0.913	75	S2
3722.805	18.12.2005	0.552	69	S2	3722.996	18.12.2005	0.919	75	S2
3722.808	18.12.2005	0.558	70	S2	3722.998	18.12.2005	0.923	74	S2
3722.811	18.12.2005	0.564	71	S2	3723.001	18.12.2005	0.928	74	S2
3722.814	18.12.2005	0.570	66	S2	3723.004	18.12.2005	0.934	75	S2
3722.817	18.12.2005	0.575	72	S2	3723.007	18.12.2005	0.940	75	S2
3722.819	18.12.2005	0.579	73	S2	3723.010	18.12.2005	0.946	74	S2
3722.831	18.12.2005	0.602	77	S2	3723.013	18.12.2005	0.951	74	S2
3722.834	18.12.2005	0.608	77	S2	3723.016	18.12.2005	0.957	74	S2
3722.836	18.12.2005	0.612	78	S2	3723.020	18.12.2005	0.965	73	S2
3722.839	18.12.2005	0.617	77	S2	3723.022	18.12.2005	0.969	72	S2
3722.842	18.12.2005	0.623	77	S2	3723.025	18.12.2005	0.974	65	S2
3722.845	18.12.2005	0.629	75	S2	3723.028	18.12.2005	0.980	70	S2
3722.848	18.12.2005	0.635	76	S2	7011.756	20.12.2014	0.097	100	S3
3722.851	18.12.2005	0.641	78	S2	7011.760	20.12.2014	0.104	98	S3
3722.854	18.12.2005	0.646	77	S2	7011.763	20.12.2014	0.110	101	S3
3722.857	18.12.2005	0.652	78	S2	7011.766	20.12.2014	0.116	102	S3
3722.860	18.12.2005	0.658	78	S2	7011.769	20.12.2014	0.122	102	S3
3722.862	18.12.2005	0.662	77	S2	7011.772	20.12.2014	0.127	101	S3
3722.865	18.12.2005	0.667	79	S2	7011.775	20.12.2014	0.133	100	S3
3722.868	18.12.2005	0.673	78	S2	7011.778	20.12.2014	0.139	101	S3
3722.871	18.12.2005	0.679	80	S2	7011.781	20.12.2014	0.145	101	S3
3722.874	18.12.2005	0.685	79	S2	7011.784	20.12.2014	0.150	100	S3
3722.878	18.12.2005	0.692	80	S2	7011.787	20.12.2014	0.156	98	S3
3722.881	18.12.2005	0.698	79	S2	7011.790	20.12.2014	0.162	97	S3
3722.884	18.12.2005	0.704	80	S2	7012.007	20.12.2014	0.578	71	S3
3722.887	18.12.2005	0.710	80	S2	7012.010	20.12.2014	0.584	72	S3
3722.890	18.12.2005	0.715	80	S2	7012.013	20.12.2014	0.590	66	S3
3722.893	18.12.2005	0.721	80	S2	7012.016	20.12.2014	0.596	55	S3
3722.896	18.12.2005	0.727	81	S2	7012.019	20.12.2014	0.601	55	S3
3722.899	18.12.2005	0.733	80	S2	7012.022	20.12.2014	0.607	58	S3
3722.901	18.12.2005	0.736	80	S2	7012.026	20.12.2014	0.615	57	S3
3722.904	18.12.2005	0.742	80	S2	7012.029	20.12.2014	0.621	57	S3
3722.907	18.12.2005	0.748	76	S2	7012.032	20.12.2014	0.626	47	S3
3722.910	18.12.2005	0.754	78	S2	7012.732	21.12.2014	0.969	90	S3
3722.913	18.12.2005	0.759	79	S2	7012.735	21.12.2014	0.975	91	S3
3722.916	18.12.2005	0.765	77	S2	7012.738	21.12.2014	0.981	91	S3
3722.919	18.12.2005	0.771	76	S2	7012.741	21.12.2014	0.987	93	S3
3722.922	18.12.2005	0.777	76	S2	7012.744	21.12.2014	0.992	94	S3
3722.925	18.12.2005	0.783	76	S2	7012.747	21.12.2014	0.998	94	S3
3722.928	18.12.2005	0.788	76	S2	7012.750	21.12.2014	0.004	94	S3
3722.931	18.12.2005	0.794	76	S2	7012.753	21.12.2014	0.010	94	S3
3722.934	18.12.2005	0.800	76	S2	7012.756	21.12.2014	0.015	95	S3
3722.937	18.12.2005	0.806	77	S2	7012.759	21.12.2014	0.021	93	S3
3722.940	18.12.2005	0.811	77	S2	7012.762	21.12.2014	0.027	95	S3
3722.943	18.12.2005	0.817	75	S2	7012.765	21.12.2014	0.033	95	S3
3722.946	18.12.2005	0.823	75	S2	7012.973	21.12.2014	0.432	89	S3
3722.949	18.12.2005	0.829	76	S2	7012.976	21.12.2014	0.438	87	S3
3722.951	18.12.2005	0.832	75	S2	7012.979	21.12.2014	0.443	84	S3
3722.954	18.12.2005	0.838	75	S2	7012.982	21.12.2014	0.449	88	S3
3722.957	18.12.2005	0.844	75	S2	7012.986	21.12.2014	0.457	87	S3
3722.963	18.12.2005	0.855	75	S2	7012.989	21.12.2014	0.462	88	S3

HJD	Date	Phase	S/N	Subset	HJD	Date	Phase	S/N	Subset
7012.992	21.12.2014	0.468	89	S3	7021.015	29.12.2014	0.862	86	S3
7012.995	21.12.2014	0.474	83	S3	7021.018	29.12.2014	0.868	85	S3
7012.998	21.12.2014	0.480	81	S3	7021.685	30.12.2014	0.148	95	S3
7013.001	21.12.2014	0.486	83	S3	7021.688	30.12.2014	0.153	93	S3
7013.772	22.12.2014	0.965	84	S3	7021.691	30.12.2014	0.159	94	S3
7013.775	22.12.2014	0.971	89	S3	7021.694	30.12.2014	0.165	97	S3
7013.778	22.12.2014	0.976	90	S3	7021.697	30.12.2014	0.171	97	S3
7013.781	22.12.2014	0.982	90	S3	7021.703	30.12.2014	0.182	97	S3
7013.784	22.12.2014	0.988	93	S3	7021.706	30.12.2014	0.188	96	S3
7013.787	22.12.2014	0.994	95	S3	7021.709	30.12.2014	0.194	97	S3
7013.791	22.12.2014	0.001	93	S3	7021.712	30.12.2014	0.199	99	S3
7013.794	22.12.2014	0.007	95	S3	7021.715	30.12.2014	0.205	97	S3
7013.797	22.12.2014	0.013	96	S3	7021.719	30.12.2014	0.213	99	S3
7013.800	22.12.2014	0.019	96	S3	7021.928	30.12.2014	0.614	100	S3
7013.803	22.12.2014	0.024	95	S3	7021.931	30.12.2014	0.620	101	S3
7013.806	22.12.2014	0.030	92	S3	7021.934	30.12.2014	0.625	100	S3
7014.013	22.12.2014	0.427	86	S3	7021.937	30.12.2014	0.631	100	S3
7014.016	22.12.2014	0.433	83	S3	7021.940	30.12.2014	0.637	99	S3
7014.019	22.12.2014	0.439	82	S3	7021.943	30.12.2014	0.643	101	S3
7014.022	22.12.2014	0.445	81	S3	7021.946	30.12.2014	0.648	101	S3
7014.025	22.12.2014	0.450	84	S3	7021.950	30.12.2014	0.656	100	S3
7014.028	22.12.2014	0.456	84	S3	7021.953	30.12.2014	0.662	101	S3
7014.031	22.12.2014	0.462	84	S3	7021.956	30.12.2014	0.668	99	S3
7014.034	22.12.2014	0.468	81	S3	7021.959	30.12.2014	0.673	101	S3
7014.038	22.12.2014	0.475	77	S3	7021.962	30.12.2014	0.679	101	S3
7014.041	22.12.2014	0.481	75	S3	7029.733	07.01.2015	0.589	60	S4
7014.044	22.12.2014	0.487	74	S3	7029.736	07.01.2015	0.595	61	S4
7019.867	28.12.2014	0.659	98	S3	7029.739	07.01.2015	0.601	62	S4
7019.870	28.12.2014	0.665	94	S3	7029.742	07.01.2015	0.607	59	S4
7019.873	28.12.2014	0.671	99	S3	7029.745	07.01.2015	0.612	61	S4
7019.876	28.12.2014	0.677	96	S3	7029.748	07.01.2015	0.618	64	S4
7019.879	28.12.2014	0.682	98	S3	7029.751	07.01.2015	0.624	62	S4
7019.882	28.12.2014	0.688	100	S3	7029.755	07.01.2015	0.632	68	S4
7019.885	28.12.2014	0.694	99	S3	7029.758	07.01.2015	0.637	71	S4
7019.889	28.12.2014	0.702	98	S3	7029.761	07.01.2015	0.643	75	S4
7019.892	28.12.2014	0.707	85	S3	7029.764	07.01.2015	0.649	82	S4
7019.895	28.12.2014	0.713	97	S3	7029.767	07.01.2015	0.655	86	S4
7019.898	28.12.2014	0.719	97	S3	7029.973	07.01.2015	0.050	80	S4
7019.901	28.12.2014	0.725	79	S3	7029.976	07.01.2015	0.056	78	S4
7020.746	29.12.2014	0.346	97	S3	7029.979	07.01.2015	0.061	75	S4
7020.749	29.12.2014	0.352	97	S3	7029.982	07.01.2015	0.067	77	S4
7020.752	29.12.2014	0.357	96	S3	7029.985	07.01.2015	0.073	74	S4
7020.755	29.12.2014	0.363	96	S3	7029.988	07.01.2015	0.079	71	S4
7020.758	29.12.2014	0.369	96	S3	7029.991	07.01.2015	0.084	71	S4
7020.761	29.12.2014	0.375	97	S3	7029.994	07.01.2015	0.090	72	S4
7020.764	29.12.2014	0.380	95	S3	7029.997	07.01.2015	0.096	75	S4
7020.767	29.12.2014	0.386	95	S3	7030.000	07.01.2015	0.102	68	S4
7020.770	29.12.2014	0.392	94	S3	7030.004	07.01.2015	0.109	71	S4
7020.773	29.12.2014	0.398	94	S3	7030.007	07.01.2015	0.115	66	S4
7020.776	29.12.2014	0.403	93	S3	7030.692	08.01.2015	0.429	98	S4
7020.780	29.12.2014	0.411	94	S3	7030.695	08.01.2015	0.435	97	S4
7020.984	29.12.2014	0.803	92	S3	7030.698	08.01.2015	0.441	98	S4
7020.988	29.12.2014	0.810	93	S3	7030.701	08.01.2015	0.447	97	S4
7020.991	29.12.2014	0.816	93	S3	7030.704	08.01.2015	0.452	97	S4
7020.994	29.12.2014	0.822	91	S3	7030.707	08.01.2015	0.458	97	S4
7020.997	29.12.2014	0.828	91	S3	7030.710	08.01.2015	0.464	97	S4
7021.000	29.12.2014	0.833	88	S3	7030.713	08.01.2015	0.470	99	S4
7021.003	29.12.2014	0.839	88	S3	7030.717	08.01.2015	0.477	97	S4
7021.006	29.12.2014	0.845	85	S3	7030.720	08.01.2015	0.483	98	S4
7021.009	29.12.2014	0.851	86	S3	7030.723	08.01.2015	0.489	98	S4
7021.012	29.12.2014	0.856	85	S3	7030.726	08.01.2015	0.495	98	S4

HJD	Date	Phase	S/N	Subset	HJD	Date	Phase	S/N	Subset
7030.932	08.01.2015	0.890	88	S4					
7030.935	08.01.2015	0.896	90	S4					
7030.938	08.01.2015	0.901	89	S4					
7030.941	08.01.2015	0.907	89	S4					
7030.945	08.01.2015	0.915	90	S4					
7030.948	08.01.2015	0.921	88	S4					
7030.951	08.01.2015	0.926	88	S4					
7030.954	08.01.2015	0.932	87	S4					
7030.957	08.01.2015	0.938	87	S4					
7030.960	08.01.2015	0.944	88	S4					
7030.963	08.01.2015	0.949	88	S4					
7030.966	08.01.2015	0.955	86	S4					
7031.689	09.01.2015	0.342	95	S4					
7031.692	09.01.2015	0.348	94	S4					
7031.695	09.01.2015	0.354	94	S4					
7031.698	09.01.2015	0.360	87	S4					
7031.701	09.01.2015	0.365	92	S4					
7031.704	09.01.2015	0.371	93	S4					
7031.707	09.01.2015	0.377	91	S4					
7031.710	09.01.2015	0.383	92	S4					
7031.713	09.01.2015	0.388	91	S4					
7031.716	09.01.2015	0.394	93	S4					
7031.719	09.01.2015	0.400	94	S4					
7031.722	09.01.2015	0.406	95	S4					
7031.928	09.01.2015	0.801	90	S4					
7031.931	09.01.2015	0.807	92	S4					
7031.934	09.01.2015	0.812	86	S4					
7031.937	09.01.2015	0.818	88	S4					
7031.940	09.01.2015	0.824	89	S4					
7031.943	09.01.2015	0.830	89	S4					
7031.947	09.01.2015	0.837	85	S4					
7031.950	09.01.2015	0.843	89	S4					
7031.953	09.01.2015	0.849	83	S4					
7031.956	09.01.2015	0.855	87	S4					
7031.959	09.01.2015	0.860	81	S4					
7031.962	09.01.2015	0.866	77	S4					
7032.689	10.01.2015	0.261	86	S4					
7032.692	10.01.2015	0.267	86	S4					
7032.695	10.01.2015	0.273	88	S4					
7032.698	10.01.2015	0.278	86	S4					
7032.701	10.01.2015	0.284	85	S4					
7032.705	10.01.2015	0.292	86	S4					
7032.708	10.01.2015	0.298	85	S4					
7032.711	10.01.2015	0.303	84	S4					
7032.714	10.01.2015	0.309	84	S4					
7032.717	10.01.2015	0.315	83	S4					
7032.720	10.01.2015	0.321	89	S4					
7032.723	10.01.2015	0.326	89	S4					
7032.930	10.01.2015	0.723	89	S4					
7032.933	10.01.2015	0.729	90	S4					
7032.936	10.01.2015	0.735	86	S4					
7032.939	10.01.2015	0.741	86	S4					
7032.942	10.01.2015	0.747	87	S4					
7032.945	10.01.2015	0.752	87	S4					
7032.948	10.01.2015	0.758	84	S4					
7032.951	10.01.2015	0.764	87	S4					
7032.954	10.01.2015	0.770	87	S4					
7032.957	10.01.2015	0.775	83	S4					
7032.960	10.01.2015	0.781	82	S4					
7032.963	10.01.2015	0.787	83	S4					
7034.929	12.01.2015	0.559	91	S4					



Fig. A.1. Observed line profiles (black dots) and their model fits (red lines) for the S1 Doppler reconstruction shown in Fig. 6. The phases of the individual observations are listed on the right side of the panels.

Fig. A.2. Fitted line profiles for the S2 Doppler reconstruction shown in Fig. 6. Otherwise as in Fig. A.1.

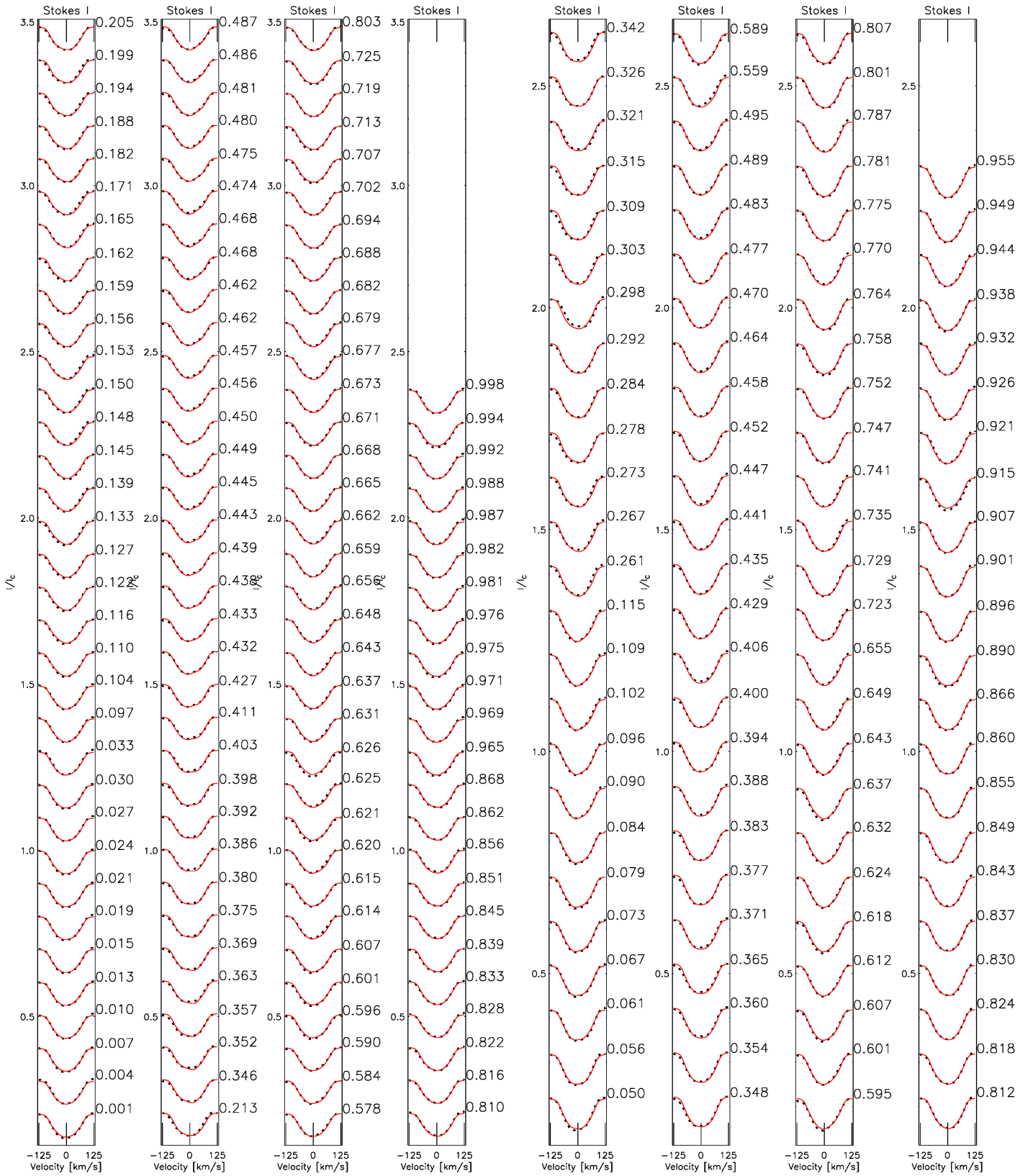


Fig. A.3. Fitted line profiles for the S3 Doppler reconstruction shown in Fig. 8. Otherwise as in Fig. A.1.

Fig. A.4. Fitted line profiles for the S4 Doppler reconstruction shown in Fig. 8. Otherwise as in Fig. A.1.